Journal of Hazardous Materials 415 (2021) 125665

Contents lists available at ScienceDirect

Journal of Hazardous Materials

journal homepage: www.elsevier.com/locate/jhazmat

Research Paper

Enhanced adsorption and degradation of methylene blue over mixed niobium-cerium oxide – Unraveling the synergy between Nb and Ce in advanced oxidation processes

Lukasz Wolski [a,*], Kamila Sobańska [b], Adrian Walkowiak [a], Kamila Akhmetova [b], Joanna Gryboś [b], Marcin Frankowski [a], Maria Ziolek [a], Piotr Pietrzyk [b,*]

[a] Faculty of Chemistry, Adam Mickiewicz University, Poznan, ul. Uniwersytetu Poznanskiego 8, 61-614 Poznan, Poland
[b] Faculty of Chemistry, Jagiellonian University, ul. Gronostajowa 2, 30-387 Kraków, Poland

ARTICLE INFO

Editor: Dr. B. Lee

Keywords:
Mixed oxides
Reactive oxygen species
Fenton-like processes
Wet peroxide oxidation
Methylene blue degradation

ABSTRACT

Formation of reactive oxygen species (ROS) via H_2O_2 activation is of vital importance in catalytic environmental chemistry, especially in degradation of organic pollutants. A new mixed niobium-cerium oxide ($NbCeO_x$) was tailored for this purpose. A thorough structural and chemical characterization of $NbCeO_x$ along with CeO_2 and Nb_2O_5 reference materials was carried out using TEM/STEM/EDS, SEM, XRD, XPS, EPR, UV–vis and N_2 physisorption. The ability of the catalysts to activate H_2O_2 towards ROS formation was assessed on the basis of EPR and Raman measurements. Catalytic activity of the oxides was evaluated in degradation of methylene blue (MB) as a model pollutant. Very high activity of $NbCeO_x$ was attributed to the mixed redox-acidic nature of its surface, which originated from the synergy between Nb and Ce species. These two properties (redox activity and acidity) ensured convenient conditions for efficient activation of H_2O_2 and degradation of MB. The activity of $NbCeO_x$ in MB degradation was found 3 times higher than that of the commercial Nb_2O_5 CBMM catalyst and 240 times higher than that of CeO_2. The mechanism of the degradation reaction was found to be an adsorption-triggered process initiated by hydroxyl radicals, generated on the surface via the transformation of $O_2^{\bullet-}/O_2^{2-}$.

1. Introduction

Advanced oxidation processes (AOPs) are the emerging most effective and economical technologies to deal with organic pollutants hardly degradable in water (Bokare and Choi, 2014). In typical AOPs, various strategies are employed to produce intermediate active oxidant radicals. One of the possible routes is decomposition of specific substrates to generate oxidizing radicals, like those produced in catalytic wet peroxide oxidation. It employs hydrogen peroxide (H_2O_2) as an oxidation source and a suitable catalyst to promote its partial decomposition into reactive oxygen species (ROS). Thus, such a catalyst exhibits a peroxidase-like activity (Liang and Yan, 2019).

Cerium dioxide (CeO_2) belongs to the most studied metal oxides in heterogeneous catalysis (Montini et al., 2016). It has been documented that ceria is successfully used not only as a support (Yang et al., 2019; Kim et al., 2012; Chen et al., 2013), but also as an active phase in numerous reactions (Wang et al., 2016; Cui et al., 2019; Ji et al., 2010; Zang et al., 2018). Among them, AOPs involving photocatalytic (Cui et al., 2019; Majumder et al., 2019) or Fenton-like oxidation processes (Ji et al., 2010; Zang et al., 2018; Hamoud et al., 2017; Cai et al., 2010; Chen et al., 2012), have attracted particular attention. The chemical reactivity of CeO_2 in oxidation reactions with the use of H_2O_2 was found to be strongly affected by ceria ability to adsorb organic pollutants (Ji et al., 2010; Zang et al., 2018; Chen et al., 2012). For instance, it has been established that efficient adsorption of acid orange 7 (AO7) dye and salicylic acid on a surface of ceria resulted in their efficient degradation (Zang et al., 2018; Chen et al., 2012), while weakly adsorbed organic species, such as methylene blue (MB) dye, were hardly degraded by H_2O_2 (Wei et al., 2019). Substantial difference in the ability of CeO_2 to adsorb these two dyes is most probably related to their various structural characteristics: AO7 is an anionic dye, while MB is classified as a cationic dye (Ong et al., 2013). The strong relationship between ceria activity in Fenton-like processes and degradation of organic pollutants stems also from a unique mechanism of hydrogen peroxide activation over CeO_2-based catalysts. The first step in this process is complexation of H_2O_2 molecules by Ce^{3+} ions that leads to the formation

* Corresponding authors.
E-mail addresses: wolski.lukasz@amu.edu.pl (L. Wolski), pietrzyk@chemia.uj.edu.pl, piotr.pietrzyk@uj.edu.pl (P. Pietrzyk).

https://doi.org/10.1016/j.jhazmat.2021.125665
Received 31 December 2020; Received in revised form 25 February 2021; Accepted 12 March 2021
Available online 15 March 2021
0304-3894/© 2021 The Authors. Published by Elsevier B.V. This is an open access article under the CC BY license (http://creativecommons.org/licenses/by/4.0/).

of peroxide species (O_2^{2-}) (Ji et al., 2010; Chen et al., 2012; Wang et al., 2014) followed by changing the sample color to brown. It was established that the as-formed peroxides are relatively chemically stable in the absence of organic contaminants and can only react with the organic substances adsorbed on the surface of ceria (Ji et al., 2010; Cai et al., 2010; Chen et al., 2012). Thus, the degradation process over cerium dioxide has been determined as a localized surface reaction that proceeds via an intermolecular rearrangement rather than a typical radical-attack (Ji et al., 2010; Cai et al., 2010; Chen et al., 2012). Yet, it is known that Ce^{3+} can also act as a scavenger of $^{\bullet}OH$ radicals and, therefore, it stabilizes the systems under oxidative stress (Łańcucki and Kruczała, 2014).

Among the alternative iron-free systems, niobium pentoxide (Nb_2O_5) is one of the most promising metal oxides utilized in AOPs (Zhao et al., 2012; Tamai et al., 2016; Prado and Oliveira, 2017). The activity of pure Nb_2O_5 in the reactions involving H_2O_2 is, however, not of the Fenton type, but it is rather connected with the electroprotic series of reactions (Ziolek et al., 2015), which lead to the simultaneous formation of surface-stabilized superoxo ($O_2^{-\bullet}$) and peroxo species, as well as free hydroxyl radicals ($H_2O_{2(aq)} + HO^-_{2(aq)} = O_2^{-\bullet}{}_{(surf)} + {}^{\bullet}OH_{(aq)} + H_2O$; $HO^-_{2(aq)} + Nb_2O_5 = O_2^{2-}{}_{(surf)} + H^+–Nb_2O_5$). Hitherto, niobia has been successfully combined with other metal oxides like W (Cardoso et al., 2012) or V/Mo (Souza et al., 2012), leading to the increased AOP activity. However, the factors promoting the activity of Nb_2O_5-based composites were found to be strongly affected by the nature of metal oxides which were mixed. Two experimental trends can be observed: (1) the increased activity due to the promotion of Fenton-like processes resulting in decomposition of H_2O_2 into $^{\bullet}OH$ and $HO_2^{\bullet}$ (the case of Nb-Fe composite (Oliveira et al., 2007)) and (2) the formation of strongly oxidizing peroxo species via reactive sorption and deprotonation of H_2O_2, like in the case of Nb-W catalysts (Cardoso et al., 2012).

Reports on the catalytic activity of ceria-doped niobia are rather meager. Up to now niobium-cerium mixed oxides have been successfully used in selective catalytic reduction of NO with NH_3 (Qu et al., 2013), dehydration of fructose (Stošić et al., 2012) or oxidative dehydrogenation of propane (Liu et al., 2016; You et al., 2017), leading to much higher catalytic activity than that observed for the parent monometallic metal oxides. It was established that the improved activity of the mixed niobium-cerium oxides in these processes resulted from their unique properties, including high surface area, higher contribution of Ce^{3+} species than that observed for parent CeO_2, and significantly higher concentration of surface active oxygen species. These species featured improved reducibility due to the presence of adjacent surface niobium. All the above-mentioned characteristics of the mixed niobium-cerium oxides make these materials interesting candidates for catalytic activation of hydrogen peroxide towards formation of ROS and degradation of the organic pollutants. However, to the best of our knowledge mixed niobium-cerium oxides have not been previously tested as catalysts in AOPs.

The overriding goal of the present study is to gain an insight into the mechanism of H_2O_2 activation and MB degradation over novel mixed niobium-cerium oxide. This model system is expected to combine the Fenton-type activity brought by incorporation of Ce^{3+}/Ce^{4+} redox couple, which is immanent to CeO_2 component, with increased sorption and acidic properties of Nb_2O_5. The research hypothesis is that the unique properties of the mixed niobium-cerium oxide will allow improvement of the efficiency of both i) generation of reactive oxygen species via H_2O_2 decomposition owing to the concerted Fenton-like and electroprotic mechanisms as well as increased concentration of Ce^{3+} ions in the lattice of the mixed oxide, and ii) degradation of methylene blue, which has been shown problematic over CeO_2-H_2O_2 system because of low adsorption of MB, resulting from low acidity of ceria surface (Wei et al., 2019). An important part of this study is also a detailed analysis of reactive oxygen species evolved upon the activation of H_2O_2 over metal oxides to get an insight into a role and nature of synergy between niobium and cerium species in AOPs.

2. Experimental

2.1. Chemicals and materials

The reagents were: niobium(V) ethoxide (Sigma-Aldrich, 99.95%), cerium(III) nitrate hexahydrate (Sigma-Aldrich; 99.99%), Nb_2O_5 CBMM (amorphous niobium pentoxide supplied by Companhia Brasileira de Metalurgia e Mineração), methylene blue (Sigma-Aldrich, dye content ≥ 82%), nitric acid (POCH, 65%, pure, p.a.), hydrogen peroxide (Sigma-Aldrich, 25–35% w/w in H_2O, for ultratrace analysis), 2-propanol (POCH, 99.8%), methanol (Sigma-Aldrich, HPLC grade, ≥99.8%), sodium azide (NaN_3, Sigma-Aldrich, ≥99.5%), p-benzoquinone (BQ, Sigma-Aldrich, ≥ 98%), ammonia solution in water (Chempur, 25%, pure p.a.), 5,5-Dimethyl-1-pyrroline N-oxide DMPO (Sigma Aldrich, ≥ 98%), o-phenylenediamine (Sigma Aldrich, ≥ 98%), deionized water. All the reagents were used without any further purification.

2.2. Synthesis of catalysts

Mixed niobium-cerium oxide ($NbCeO_x$) was synthesized using a facile co-precipitation method. In a typical synthesis route, niobium(V) ethoxide (13.3648 g, 0.042 mol) and cerium(III) nitrate hexahydrate (18.2372 g, 0.042 mol) were dissolved in 250 mL of methanol and 250 mL of deionized water, respectively. Next, the aqua solution of cerium (III) nitrate hexahydrate was poured into the solution containing niobium(V) ethoxide and methanol upon vigorous stirring. After 30 min of agitation, the as-obtained mixture was added upon intensive stirring into aqua ammonia solution (250 mL) and agitated for the next 60 min. Next, the precipitate was separated by filtration, washed with deionized water (500 mL) and dried at 120 °C for 24 h. The as-prepared dry powder was crushed in agate mortar and calcined at 500 °C for 5 h (temperature ramp: 2 °C/min) leading to the formation of the catalyst labeled as $NbCeO_x$.

Monometallic oxides, namely CeO_2 and Nb_2O_5, were prepared as reference materials according to the same procedure. In a typical synthesis of monometallic oxides, the amount of each metal source was increased to 0.084 mol (i.e. 26.7296 g of niobium(V) ethoxide and 36.4745 g of cerium(III) nitrate hexahydrate, respectively) to keep the same quantity of metal ions in all the reaction mixtures.

2.3. Characterization of materials

The X-ray powder diffraction (XRD) measurements were carried out with a D8 Advance diffractometer (Bruker) using Cu Kα radiation (λ = 0.154 nm). The XRD patterns were acquired with a step size of 0.02° in the 2Θ range of 10–80°.

Raman spectra were recorded in ambient conditions (air, room temperature) using a Renishaw InVia dispersive spectrometer equipped with a CCD detector and integrated with a Leica DMLM confocal microscope. The used laser excitation wavelength was 785 nm and the laser power at the sample position was adjusted to 1.5 mW. The Raman scattered light was collected in the spectral range 100–1500 cm^{-1} with a 50× magnification lens. At least five scans were accumulated to ensure a sufficient signal-to-noise ratio. The spectra were processed using the Wire 2.0 software.

The N_2 adsorption-desorption isotherms were obtained at –196 °C using a Micromeritics ASAP 2020 Physisorption Analyzer. Before the measurements, samples were degassed at 120 °C for 10 h. The surface area was calculated assuming the BET method and the average pore size was estimated from the adsorption branch using BJH method.

The morphology, structure, chemical and phase composition of the investigated materials were analyzed on the basis of electron microscopy observations. The morphology was investigated with a scanning electron microscope (SEM) Quanta FEG 250 (FEI) operated at the accelerating voltage of 5 kV. Energy-dispersive spectroscopic (EDS) analyses were performed at the accelerating voltage of 20 kV using EDS

Octane Silicon Drift Detector (EDAX). Conventional and scanning transmission electron microscopy (TEM/STEM) measurements were carried out using a Tecnai Osiris instrument (FEI/Thermo Fisher) with an X-FEG Schottky field emitter operating at accelerating voltage of 200 kV. The particle size analysis was performed using the DigitalMicrograph software (from Gatan Microscopy Suite Software). The Z-contrast imaging was performed using a High Angle Annular Dark Field (HAADF) detector in the scanning mode. Chemical analysis was carried out using super-X EDX (Energy Dispersive X-ray) system with the windowless 4-sector silicon drift detector (SDD). EDX elemental mapping was made with a sample drift correction using the Bruker Esprit software. Prior to the microscopic imaging, the samples were dispersed on lacey carbon-coated copper grid (Agar Scientific, 300 mesh).

Diffuse reflectance UV–vis spectra (DR UV–vis) were recorded with a Varian Cary 300 Scan spectrophotometer equipped with a diffuse reflectance accessory. The spectra were recorded at room temperature in the range 200 – 800 nm. Spectralon was used as the reference material.

X-ray photoelectron spectroscopy (XPS) analyses were performed using an ultra-high vacuum photoelectron spectrometer based on Phoibos150 NAP analyzer (Specs, Germany). The analysis chamber was operated under vacuum with a residual pressure of 5×10^{-9} mbar and the sample was irradiated with a monochromatic Al Kα (1486.6 eV) radiation. Any charging that would occur during the measurements was compensated for by shifting the entire spectrum by a distance needed to set the binding energy of the C1s, assigned to adventitious carbon, to the reference value of 284.8 eV. Deconvolution of XPS spectra was performed using the CasaXPS software.

Electron paramagnetic resonance (EPR) spectra were recorded with an X-band Bruker ELEXSYS-580 spectrometer, operating at 100 kHz field modulation and employing 0.1 mT modulation amplitude. Prior to the measurements of the solids, the samples were sealed in quartz tubes, and outgassed in a vacuum line ($p < 10^{-3}$ mbar) for 2 h at room temperature. The spectra were recorded at room temperature. For qualitative spin trapping experiments a small amount (0.2 mg) of an oxide was contacted with an aqueous mixture of 0.25 mL of 1% H_2O_2 and 0.5 mL of 4 mg/mL DMPO. The obtained solution was next transferred to a quartz capillary, and the EPR spectra were recorded at room temperature. In the case of singlet oxygen detection, 2,2,6,6-tetramethyl-4-piperidone (TEMP) was used as a selective chemical probe (Díaz-Uribe et al., 2014). A portion of 0.5 mL of 20 mM TEMP solution was mixed with 0.1 mL of the catalyst suspension and 0.1 mL of 1% H_2O_2 solution. The EPR parameters of the resultant spin adducts and the surface radicals were determined by computer simulations of the experimental spectra using the EPRsim32 software (Spałek et al., 2005).

The concentration of dissolved oxygen that evolved upon H_2O_2 decomposition was monitored using an inoLab Multi 9430 IDS setup, equipped with a fluorescent probe FDO 925 (WTW, Poland). During the measurement, the probe was immersed in a suspension containing 10 mg oxide, 100 mL of deionized water and 1 mL of 30% H_2O_2. The amount of oxygen was measured as a function of time.

2.4. Test reactions

To screen the acid-base properties of the investigated oxides, conversion of 2-propanol (dehydration and dehydrogenation reactions) was measured using a microcatalytic pulse reactor. The catalyst bed (0.05 g of the size fraction of $0.5 < Ø < 1$ mm) was first activated at 350 °C for 2 h under nitrogen flow (40 mL/min). The reaction was carried out at 200 °C and 250 °C using 3 μL pulses of 2-propanol under nitrogen flow (65 mL/min). The substrate and the reaction products (propene, 2-propanone, and diisopropyl ether) were analyzed on-line using a gas chromatograph (SRI model 8610 C) with FID detection. The reaction mixture was separated on a chromatographic column supplied by Chromatography Research Supplies, Inc. (matrix: Chromosorb W-AW, 60/80 mesh; matrix active group: 5% Carbowax, 20 M phase). The column was heated according to the following program: 4 min at 47 °C, temperature increase to 120 °C (heating rate of 40 °C/min), 5 min at 120 °C.

The peroxidase type activity was tested by measuring the absorbance of the oxidation product of the peroxidase substrate (o-phenylenediamine, OPD) in the presence of H_2O_2. Measurements were carried out using a Cary 60 spectrophotometer (Agilent Technologies) with a 10 mm cuvette. The experiments were carried out using approximately 0.1 mg of the catalyst, with the final concentrations of 1.2 mM OPD and 0.3 M H_2O_2. The spectra were recorded in the spectral range 200 – 800 nm every 3 min, with a wavelength step of 1 nm, and an average counting time of 0.2 s per point.

The activities of the investigated oxides in generation of ROS were evaluated using discoloration of methylene blue (MB) at room temperature as a distinctive test reaction. In a typical test, 0.020 g of the catalyst was dispersed in 80 mL of MB aqueous solution ($C_{MB} = 12$ mg/L). Then, 200 μL of H_2O_2 were added. In order to avoid MB photocatalytic degradation, the reactions were performed in a dark chamber. The dye discoloration was monitored using UV–vis spectroscopy (Varian, Cary 300 UV–vis spectrophotometer). For this purpose, the 4 mL aliquots of the reaction mixture were taken at defined time steps, and the catalyst was separated from the solution by filtration through a 0.2 μm Millipore filter. For the sorption capacity measurements pure water solution was used instead of H_2O_2. The pH of the reaction mixtures was adjusted using diluted HNO_3 aqueous solution. The involvement of ROS in MB discoloration was additionally probed by adding specific quenchers, i.e. methanol and 2-propanol (for hydroxyl radicals), sodium azide (NaN_3, for singlet oxygen) and p-benzoquinone (BQ, for superoxide radical anions). Typically, a given amount of the quencher (as indicated in the figures) was added to a mixture composed of 80 mL of MB ($C_{MB} = 12$ mg/L), 20 mg of the catalyst and 200 μL of H_2O_2. In these tests pH was adjusted to 5.1 using diluted HNO_3 aqueous solution.

Products of MB degradation were identified with the use of a quadrupole time of flight (QTOF) mass spectrometer (Impact HD, Bruker) in positive ion mode. The reaction mixtures were diluted 100 times prior to the analysis. The diluted reaction samples were injected into the ESI source with a syringe pump at a flow rate of 3 μL/min. The ESI conditions were as follows: heated capillary temperature of 200 °C, sheath gas (N_2) at a flow rate of 4 L/min, capillary voltage of 3600 V. The corroborative measurements of total carbon (TC) content were performed using a Total Organic Carbon analyzer (TOC-L) (Shimadzu, Japan).

3. Results

3.1. Structural and textural characterization

Fig. 1A shows XRD patterns acquired for the synthesized oxides. Both niobia and ceria exhibited well-defined crystalline structures which can be identified on the basis of the indexed diffractograms. The XRD pattern of niobium pentoxide corresponds to the hexagonal structure (ICDD No. 00–007–0061; Fig. S1, Supplementary Data), while cerium dioxide exhibited the cubic cerianite structure (ICDD No. 00–034–0394; Fig. S1). Interestingly, in the case of the mixed niobium-cerium oxide, no reflexes due to the crystalline niobium pentoxide were identified, suggesting the formation of either highly dispersed or amorphous oxide phases. The XRD pattern of $NbCeO_x$ oxide exhibits only broadened reflexes arising from the cubic cerianite structure. Such a broadening of XRD peaks may arise not only from smaller crystallite size of ceria particles in the mixed oxide, but also from the presence of an additional $CeNbO_4$ phase. Indeed, as can be seen in Fig. 1B, the main diffraction peaks of cubic cerianite structure coincide well with the most intense peaks characteristic of tetragonal $CeNbO_4$ phase. The above observation implies that precise analysis of chemical composition of the mixed oxide is not possible solely on the basis of XRD results. Therefore, more detailed phase characterization was made and an insight into the structure of the mixed oxide was obtained on the basis of the high-resolution TEM and selected area electron diffraction (SAED)

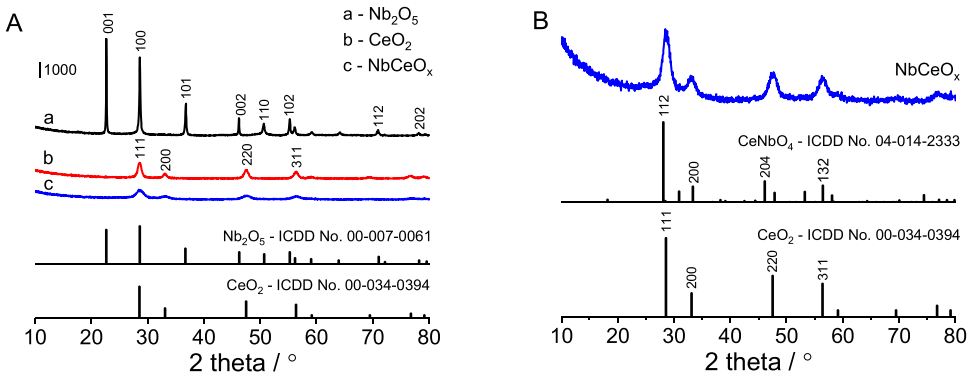


Fig. 1. (A) Experimental XRD patterns of Nb_2O_5, CeO_2 and mixed-oxide $NbCeO_x$ catalysts, (B) comparison of powder database XRD patterns of $CeNbO_4$ (ICDD No. 04–014–2333) and CeO_2 (ICDD No. 00–034–0394) with experimental diffractogram of $NbCeO_x$.

techniques.

The general morphology of the investigated powder samples was studied with the scanning electron microscopy (SEM). As can be seen in Fig. S2, both CeO_2 and $NbCeO_x$ exhibit similar morphologies. The samples consist of large (micrometric scale), irregular aggregates of crystalline particles. Yet, the crystals (agglomerates) of $NbCeO_x$ are clearly fused into a porous structure. In contrast, the sample of Nb_2O_5 has a cauliflower-like morphology. In micrometric scale, an analysis of elements' distribution (Nb and Ce) in the mixed oxide reveals that both elements were mostly homogeneously distributed, and the assumed

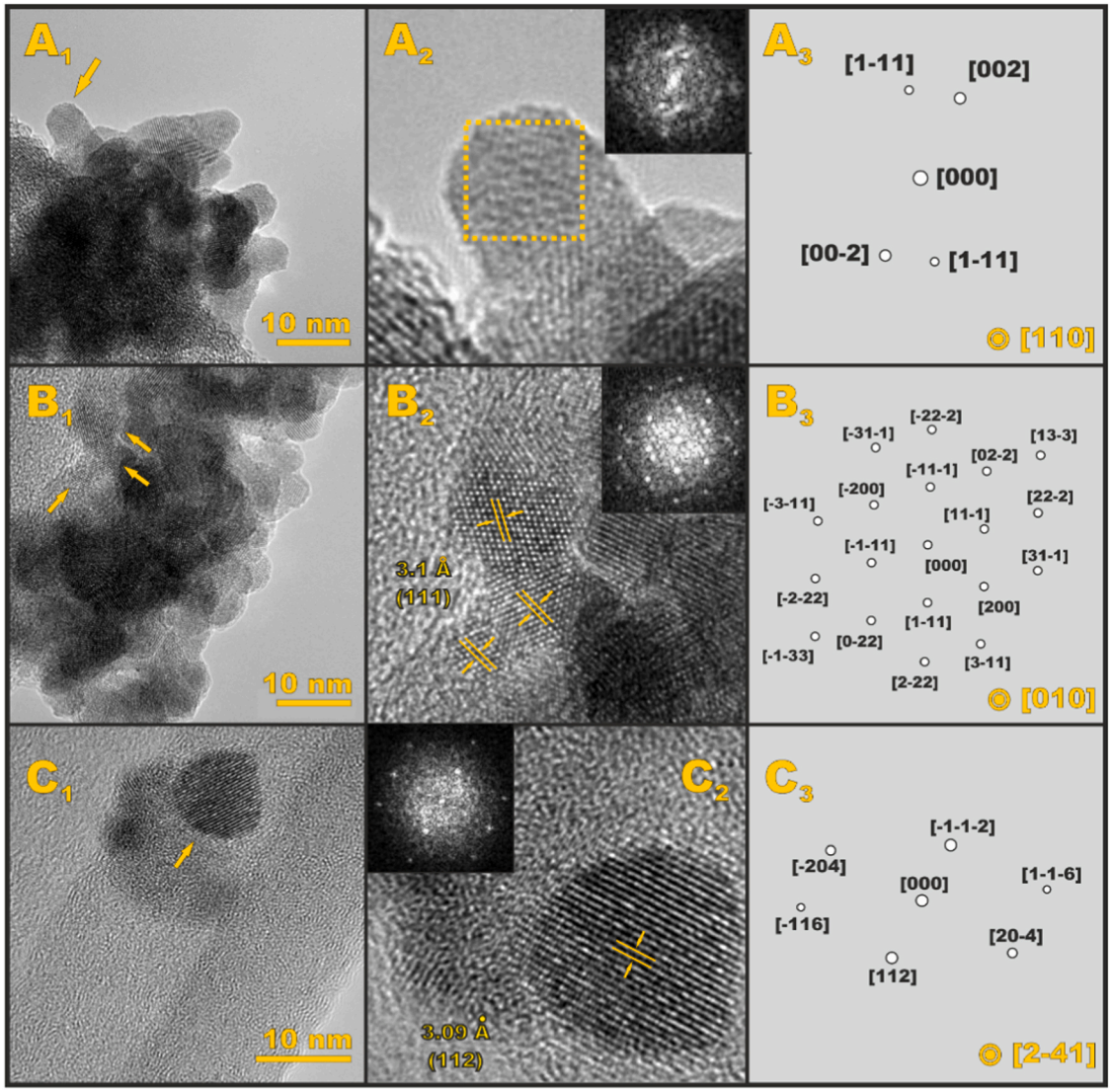


Fig. 2. TEM images (columns 1 and 2) and selected area electron diffraction (SAED) patterns (column 3) of mixed $NbCeO_x$ oxide showing identified phases of (A) Nb_2O_5, (B) CeO_2, and (C) $CeNbO_4$.

atomic ratio Nb:Ce of 1:1 was preserved. However, it is worth noting that some small regions with slightly higher concentration of niobium or cerium species were also identified (see Fig. S3, Supplementary Data).

Detailed structural analysis of the crystal phases included in the mixed $NbCeO_x$ oxide was performed with high-resolution TEM and SAED techniques. Fig. 2 presents conventional TEM images of various parts of the same mixed oxide sample, comprising individual nanocrystals of Nb_2O_5 (Fig. 2A_1), CeO_2 (Fig. 2B_1), and binary $CeNbO_4$ oxide (Fig. 2 C_1) (Liu et al., 2016). The nanocrystals selected for further analysis are marked with yellow arrows. Their enhanced-resolution images with well exposed lattice fringes are shown in Fig. 2 A_2,B_2,C_2. To assign the phase and orientation of the nanocrystals, the calculated Fourier patterns (FFT) were used (see inserts in Fig. 2 A_2,B_2,C_2). For CeO_2 (Fig. 2 B_2) and binary $CeNbO_4$ oxide (Fig. 2C_2) the characteristic spacing for (111) and (112) lattices, respectively, is marked. For the sake of clarity, the calculated FFT patterns together with the assigned diffraction planes are also shown separately in the third column of Fig. 2.

SAED analysis of the $NbCeO_x$ sample revealed the co-presence of three individual, yet tightly agglomerated, phases of CeO_2, $CeNbO_4$ and Nb_2O_5, constituting well mixed aggregates (as observed in SEM, Fig. S2). Apart from assigning the phases, FFT analysis allowed also determination of the orientation of the analyzed nanocrystals, e.g. [010] for CeO_2, [2-41] for $CeNbO_4$, and [110] for Nb_2O_5.

Fig. 3A,B shows typical conventional and high resolution TEM images of individual $CeNbO_4$ nanocrystals identified on the basis of the characteristic SAED pattern (Fig. 3C) (Santoro et al., 1980) recorded for the $NbCeO_x$ catalyst. The nanocrystals exhibit euhedral morphology and are strongly agglomerated. The HAADF STEM image followed by EDS elemental mapping (Fig. 3E_1–E_4) confirmed prevalent formation of pure $CeNbO_4$ phase (with Nb:Ce atomic ratio of 1:1 calculated from EDS peaks, see Fig. S4a, Supplementary Data).

The results obtained for the reference CeO_2 catalyst are presented in Fig. S5, Supplementary Data. The TEM images show strong agglomeration of the nanocrystals of euhedral morphology. The FFT pattern confirms the presence of CeO_2 phase composed of nanocrystal oriented along the (011) axis (Artini et al., 2015). The HAADF STEM image and EDS elemental mapping (Fig. S5) revealed chemical composition of the sample as CeO_2, however, the EDS method is unreliable for the detection of defect sites (connected with the presence of Ce^{3+}) and a possible non-stoichiometry. These aspects are discussed below on the basis of the results obtained with XPS and EPR techniques.

Particle size analysis of the STEM images of the mixed oxide (Fig. S6, Supplementary Data) shows that the nanocrystals constituting $NbCeO_x$ exhibit the average diameter of 8.1 nm (maximum size 17.4 nm, minimum size 4.5 nm, standard deviation 2.4 nm), whereas the co-existing Nb_2O_5 nanocrystals are the smallest, with poorly developed morphology and crystallinity. Nanocrystals of CeO_2 used as a reference, have the average diameter equal to 10.1 nm (maximum size 17.7 nm, minimum size 5.2 nm, standard deviation 2.6 nm).

The morphological analysis of the investigated catalysts was supported by textural parameters derived from the analysis of nitrogen adsorption-desorption isotherms (Fig. 4A). CeO_2 and $NbCeO_x$ exhibit isotherms of type IV(a) characteristic of the porous materials with hysteresis loop classified according to IUPAC convention as H2(b) (Thommes et al., 2015). The shape of this hysteresis loop is associated with pore blocking effects and indicates the presence of the mesopores with large distribution of neck widths. The isotherm of Nb_2O_5 resembles that of type III with a small hysteresis loop of type H3, which is characteristic of the macroporous materials (Thommes et al., 2015).

The porosities of CeO_2 and $NbCeO_x$ remained similar, yet with some slight differences. For $NbCeO_x$, the hysteresis loop results mainly from the capillary condensation within the relatively uniform mesopores. For CeO_2 the adsorption and desorption curves show no parallel section, which clearly indicates narrowing of the pores near their openings. Fig. 4B shows a detailed analysis of pore size distribution. The surface area and the average pore size estimated from the nitrogen adsorption-desorption isotherms are summarized in Table 1. Both materials show similar pore size distribution in the range from 2 to 20 nm and comparable average pore size of ca. 5 nm. The largest surface area of 102 m^2/g was obtained for the mixed niobium-cerium oxide. This value was approximately twice as large as that calculated for CeO_2, and more than 10 times larger than that found for crystalline Nb_2O_5.

3.2. Electronic structure and redox properties

The electronic structure of the studied catalysts was assessed with UV–vis spectroscopy. Fig. 5A shows the spectrum recorded for Nb_2O_5 which exhibits a broad absorption band with maximum intensity at ca. 290 nm and a shoulder at ca. 230 nm. The former band has been attributed to the octahedrally coordinated niobium species (charge-transfer transition from O^{2-} to Nb^{5+} (Nowak and Jaroniec, 2008)), while the latter has been assigned to the tetrahedrally coordinated niobium

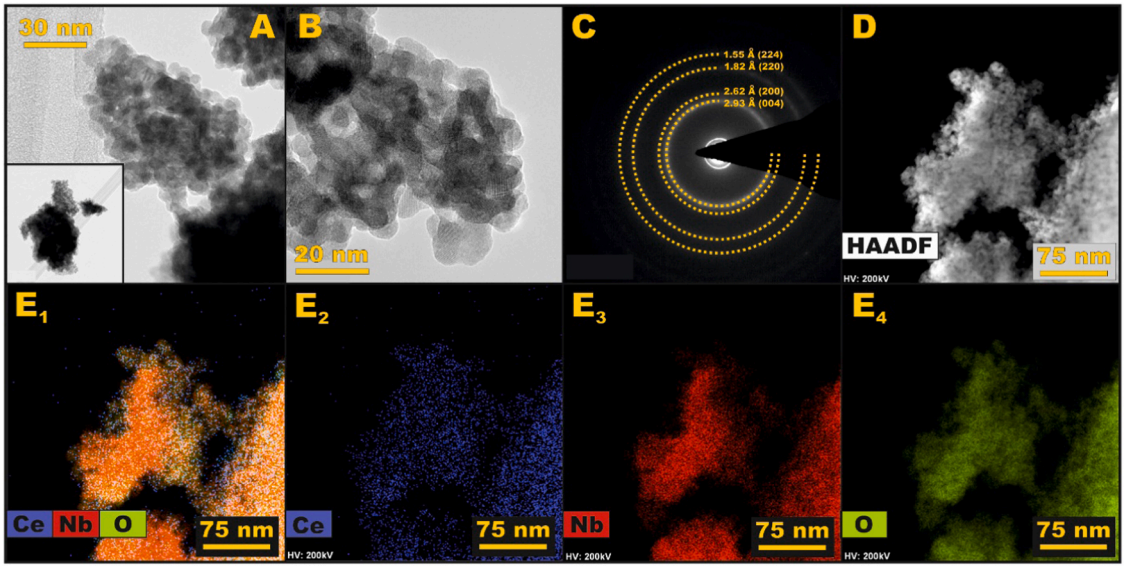


Fig. 3. TEM/EDS analysis of chemical composition of individual binary $CeNbO_4$ oxide nanocrystals. (A) Conventional and (B) HR-TEM images, (C) SAED pattern of nanocrystals shown in figure (A). (D) HAADF image along with EDS elemental mapping (E_1 – E_4).

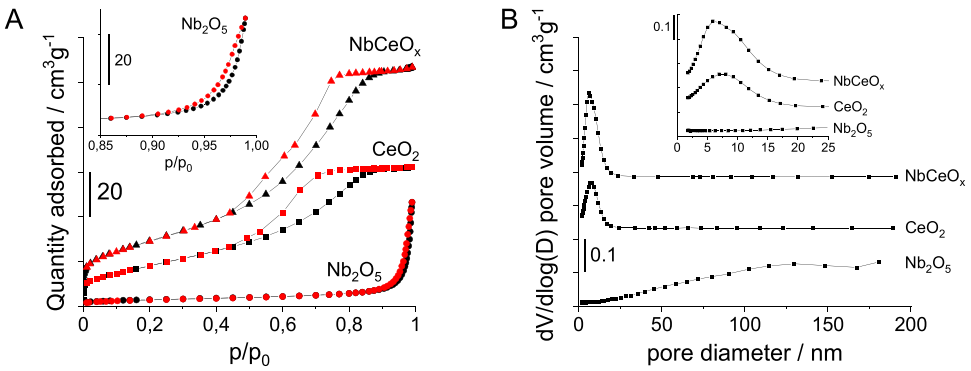


Fig. 4. (A) Nitrogen adsorption-desorption isotherms of catalysts and (B) pore size distribution estimated from adsorption branch of N_2 isotherms using BJH method.

Table 1
Physicochemical characteristics of investigated catalysts.

Catalyst	BET [m^2/g]	Average pore size[a] [nm]	Oxidation state of Nb[b]		Oxidation state of Ce[b]	
			Nb^{5+}	Nb^{4+}	Ce^{4+}	Ce^{3+}
Nb_2O_5	11	31.3	100%	–	–	–
$NbCeO_x$	102	5.5	60%	40%	74%	26%
CeO_2	64	5.1	–	–	82%	18%

[a] estimated from adsorption branch of N_2 isotherms using BJH method
[b] relative contributions of niobium or cerium species estimated from deconvoluted XPS data

species (Ziolek et al., 2012).

The UV–vis spectrum of CeO_2 exhibits two well resolved absorption bands with maxima at 342 and 267 nm. According to literature (Liu et al., 2010; Reddy et al., 2008), these bands are attributed to the $O^{2-} \rightarrow Ce^{4+}$ charge-transfer transition and the interband transition, respectively. It is important to notice that the band due to the $O^{2-} \rightarrow Ce^{3+}$ charge-transfer transition (observed usually at 255 nm (Liu et al., 2010; Aboukaïs et al., 2016)) is not well pronounced in the CeO_2 spectrum. However, owing to the large bandwidths and a possible overlapping with the band typical of the interband transition, the presence of Ce^{3+} species cannot be excluded solely on the basis of the UV–vis spectra. More detailed analysis of the presence of Ce^{3+} with XPS and EPR techniques is presented below.

The mixed niobium-cerium oxide exhibits clearly different optical properties than those observed for Nb_2O_5 and CeO_2 (Fig. 5A). It confirms the presence of strong chemical interactions between ceria and niobia, which resulted in the formation of a new entity. As compared to the spectrum of CeO_2, the intensity of the band at 267 nm is significantly reduced and the absorption edge is red-shifted. According to literature (Zhang and Lin, 2011), such a red-shift results from the formation of oxo-bridged bimetallic linkages (e.g. Zr^{IV}–O–Ce^{III}). Formation of such structures has been previously reported in literature and interpreted as a result of the metal-to-metal charge-transfer transition (MMCT) in various oxo-bridged bimetallic systems including Ti^{IV}–O–Ce^{III} (Nakamura et al., 2007), Ti^{IV}–O–Fe^{II} (Okamoto et al., 2008) and Ti^{IV}–O–Mn^{III} (Sun and Lin, 2009). Taking into account these reports, we attributed the observed red-shift of the UV–vis band of the mixed oxide to the development of MMCT transitions resulting from the presence of the Nb^{IV}–O–$Ce^{IV} \leftrightarrow Nb^{V}$–O–$Ce^{III}$ redox pairs. Formation of the redox pairs of the bimetallic oxo-bridged systems will be further discussed when analyzing the XPS data.

The band gap energy determined by the Tauc's method (Fig. 5B) confirms that the mixed oxide is characterized with the presence of specific chemical interactions between CeO_2 and Nb_2O_5 phases forming the binary system (as discussed based on TEM/EDS). The E_g value obtained for $NbCeO_x$ (2.28 eV) is clearly below all values characteristic of CeO_2 (2.61 eV) and Nb_2O_5 (3.11 eV).

To get a deeper and more local insight into the oxidation state of the surface metals and the interactions between the individual components of the mixed oxide, X-ray photoelectron spectroscopy (XPS) study was applied. Detailed analysis of the Nb 3d spectrum recorded for Nb_2O_5 allowed distinguishing two spectral components corresponding to the binding energies (BE) of 207.1 and 209.8 eV (Fig. 6A). These two peaks are characteristic of Nb^{5+} species in Nb_2O_5 (spin orbitals Nb $3d_{5/2}$ and Nb $3d_{3/2}$, respectively) (Kong et al., 2016). Analysis of Nb 3d spectrum recorded for the mixed oxide was more complex because the peaks characteristic of niobium species are overlapped with the spectral component typical of cerium (spin orbital Ce $4p_{3/2}$; see Fig. 6A). Detailed deconvolution of the spectrum permitted distinction of several peaks which have been attributed to Nb^{5+} (BE of 207.1 and 209.8 eV), Nb^{4+} (BE of 205.8 and 208.6 eV) and Ce 4p (206.2 and 220.1 eV) (You et al., 2017; Li et al., 2016; Liu et al., 2015). The estimated contribution of Nb^{4+} species in $NbCeO_x$ sample was 40% of all niobium surface

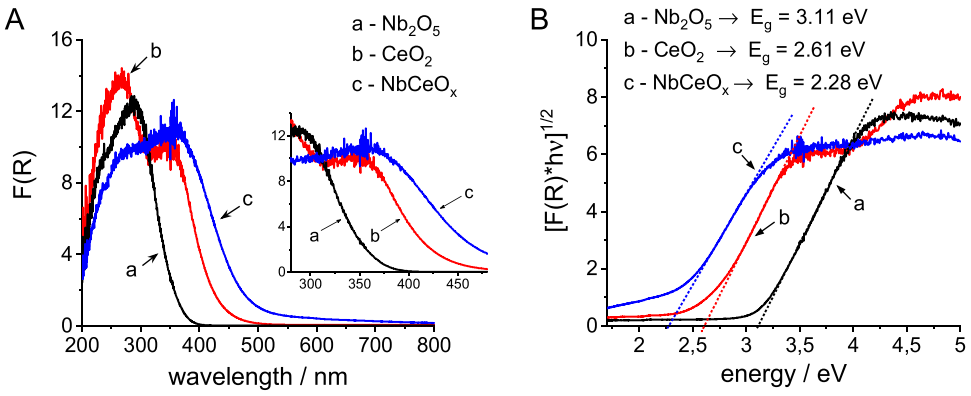


Fig. 5. (A) UV–vis spectra of Nb_2O_5, CeO_2 and mixed $NbCeO_x$ catalysts and (B) Tauc's plots for determination of band gap energy (E_g – optical band gap).

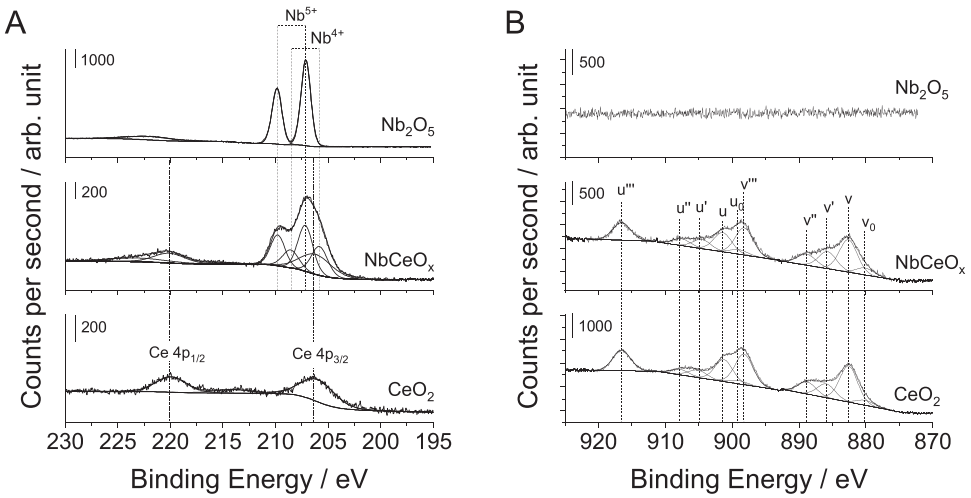


Fig. 6. (A) Nb 3d + Ce 4p and (B) Ce 3d XPS spectra of Nb_2O_5, $NbCeO_x$ and CeO_2 catalysts.

species (see Table 1).

According to literature (Bêche et al., 2008; Maslakov et al., 2018), analysis of the Ce 3d spectra recorded for CeO_2 and $NbCeO_x$ (Fig. 6B) was carried out by deconvolution of the signals into two sets of components, namely v_0, v, v', v'', v''', and u_0, u, u', u'', u'''. The components labeled as v, v'', v''' and u, u'', u''' are assigned to Ce^{4+} species, while v_0, v′ and u_0, u′ are attributed to Ce^{3+} species (Bêche et al., 2008; Pereira-Hernández et al., 2019). The obtained results collected in Table 1 show that the relative contribution of Ce^{3+} ions in $NbCeO_x$ sample was significantly higher than that observed for CeO_2 (18% for CeO_2 vs. 26% for $NbCeO_x$).

3.3. Acid-base properties

Acid-base properties of the surfaces of the investigated catalysts were examined in 2-propanol dehydration and dehydrogenation as test reactions. The dehydration of 2-propanol to propene requires the presence of acidic centers (Lewis or Brønsted) (Gervasini et al., 1997), di-isopropyl ether is formed with the participation of the Lewis acid-base pair centers, whereas the dehydrogenation to acetone occurs on the base (Gervasini et al., 1997) and/or redox sites (Lahousse et al., 1994). The selectivity of the catalysts at similar conversions of 2-propanol is summarized in Table 2.

It was found that the main products of the reaction catalyzed with Nb_2O_5 were propene and di-isopropyl ether (selectivity of 74% and 18%, respectively), while CeO_2 exhibited very high selectivity to acetone (~100%). These results clearly revealed that Nb_2O_5 and CeO_2 were completely different in terms of surface chemical properties. Niobia surface was found to be acidic with some contribution of basic surface oxygens, whereas ceria exhibited basic/redox properties. In the case of the mixed niobium-cerium oxide, $NbCeO_x$, the main product of 2-propanol dehydration and dehydrogenation was acetone (77%), but propene and di-isopropyl ether were also identified (selectivity of 15% and 8%, respectively). Only traces of propene and di-isopropyl ether were detected during the test reaction with CeO_2. Therefore, $NbCeO_x$ showed significantly higher acidity than CeO_2, preserving the redox properties originating from the presence of the redox couples detected with XPS.

Table 2
Results of 2-propanol dehydration and dehydrogenation over catalysts used in this study presented for similar alcohol conversion.

Catalyst	Temperature [°C]	Conversion [%]	Selectivity [%]		
			Propene	Acetone	Di-isopropyl ether
Nb_2O_5	250	3	74	8	18
CeO_2	250	3	traces	~100	traces
$NbCeO_x$	200	5	15	77	8

3.4. Surface species

The presence of surface-trapped species formed during the reaction of H_2O_2 solution with catalysts' surfaces was probed with micro-Raman spectroscopy. The full range spectra of pristine oxide samples are collected in Fig. S7, Supplementary Data. The Raman spectrum of CeO_2 exhibits one band at 466 cm^{-1} which is assigned to the F_{2g} vibration (Schilling et al., 2017). It is associated with the stretching of the Ce–O bonds. In the spectrum of crystalline niobia a broad band at about 705 cm^{-1} and a weak shoulder near 830 cm^{-1} are visible. They are assigned to the symmetric stretching within niobia polyhedra and to the symmetric stretching mode of the surface $O^{=}Nb^{=}O$ species, respectively. Additional bands appearing between 200 and 350 cm^{-1} are characteristic of the bending modes of Nb–O–Nb linkages (Brayner and Bozon-Verduraz, 2003). The spectrum of $NbCeO_x$ mixed oxide shows a band at 466 cm^{-1}, similar to that in the spectrum of ceria, but with smaller intensity. Thus, the Raman results are entirely consistent with XRD data (Fig. 1).

After treatment with H_2O_2 solution all features of Raman spectra remained, indicating preservation of the previously identified crystalline phases. However, additional bands appeared in the range of 830 – 870 cm^{-1} (Fig. 7). As a reference for the bands attribution we used an amorphous sample of Nb_2O_5 CBMM, since this material had been shown to be active in H_2O_2 decomposition via the electroprotic mechanism leading to the vast accumulation of surface ROS (both peroxo and superoxo) (Ziolek et al., 2015). The Raman band located at 873 cm^{-1} is characteristic of a surface peroxo group O_2^{2-} (Wachs and Roberts, 2010). Bands of similar origin, yet differing in intensity, are observed for CeO_2 (840 cm^{-1}) and $NbCeO_x$ (864 cm^{-1}) oxides. The observed pronounced shift of the three frequencies results from the variation of degree of ionicity of the bond formed between peroxo species and the adsorption centers. Thus, the highest local ionicity of the surface centers is observed for CeO_2 surface. At the same time, the peroxo band has the lowest intensity for ceria. Additionally, in the case of the mixed $NbCeO_x$, treatment with H_2O_2 leads to a decrease in intensity of the 600 cm^{-1} band (which is related to the presence of defected sites associated with oxygen vacancies). No new bands were observed for crystalline Nb_2O_5 upon interaction with H_2O_2.

Apart from the diamagnetic peroxo species, the paramagnetic ones were probed with EPR spectroscopy. The resulting spectra are shown in Fig. 8. The EPR spectra recorded for amorphous niobium oxide (Nb_2O_5

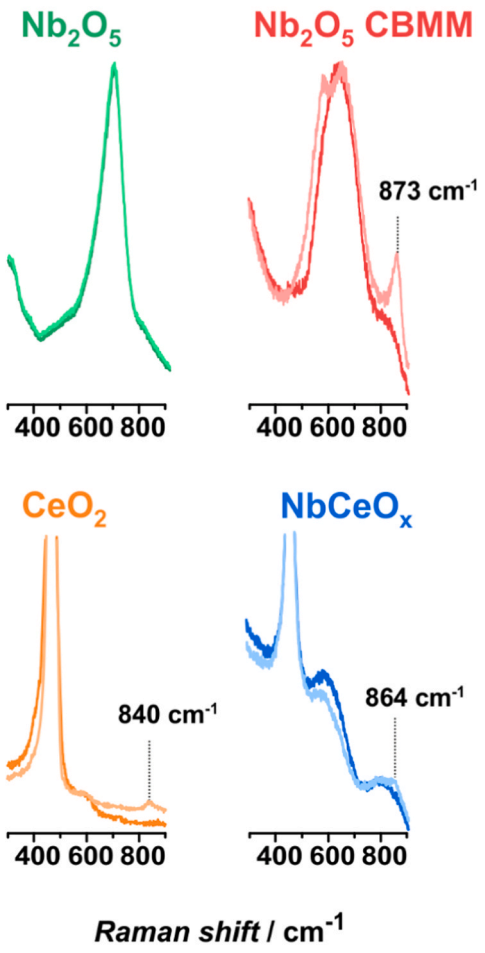


Fig. 7. Raman spectra of Nb_2O_5, amorphous Nb_2O_5 CBMM, CeO_2, and $NbCeO_x$ oxides before (bright lines) and after (pale lines) treatment with H_2O_2 solution and subsequent drying in air. Positions of bands due to peroxo species are indicated.

CBMM) and mixed $NbCeO_x$ after treatment with H_2O_2 exhibit a complex orthorhombic signal. A clearly resolved hyperfine structure due to the interaction with ^{93}Nb nucleus ($I = 9/2$, 100%) is visible. The presence of such a splitting indicates direct bonding of a radical to the metallic center (Nb^{5+}). The spin-Hamiltonian parameters obtained by computer simulation: $g_{xx} = 1.9930$, $g_{yy} = 2.0170$, $g_{zz} = 2.0320$, $|A_{yy}| = 1$ mT (A_{xx} and A_{zz} components unresolved), are indicative of the surface-trapped superoxo (O_2^-) species (Sobańska et al., 2015). An analogous signal is observed for the reference amorphous Nb_2O_5 CBMM, but in this case it is more intense than that for $NbCeO_x$. In addition, another signal which can be assigned to the reduced Ce^{3+} cations ($g_\perp = 1.9625$, $g_{||} = 1.9370$) is observed for the mixed oxide. Its attribution is based on the similar spectra recorded for CeO_2 (Fig. 8) (Ansari et al., 2014). Thus, the EPR results remain in agreement with the XPS data (see above). Note that the signal assigned to Ce^{3+} is recorded before and after treatment with H_2O_2, however, the reaction of Ce^{3+}, which is present at $NbCeO_x$ surface, with hydrogen peroxide leads to the partial oxidation of cerium(III) evidenced with the decreasing intensity of the EPR signal.

3.5. H_2O_2 decomposition and ROS identification

Generation of hydroxyl radicals ($^\bullet$OH) via decomposition of H_2O_2 upon interaction with a suitable catalyst proves its peroxidase-like activity. The EPR spectra recorded for the assays composed of the investigated oxides (CeO_2, $NbCeO_x$, and Nb_2O_5 CBMM) dispersed in H_2O_2 solution in the presence of DMPO spin trap are shown in Fig. 9A. In all

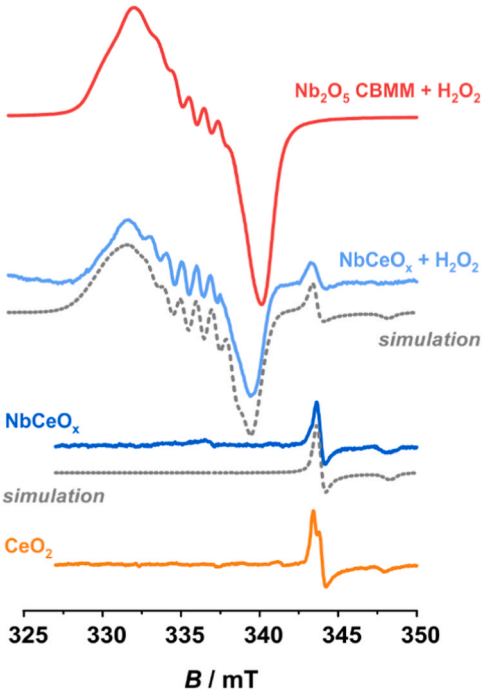


Fig. 8. Solid-state X-band EPR spectra (liquid nitrogen temperature) of amorphous Nb_2O_5 CBMM, $NbCeO_x$, and CeO_2 oxides. After treatment with H_2O_2 solution (when indicated) samples were dried in air.

cases, a quartet signal composed of four lines (hyperfine interaction due to ^{14}N ($I = 1$) and ^1H ($I = 1/2$) nuclei), with relative integral intensities of 1:2:2:1, is observed. The spin-Hamiltonian parameters obtained by computer simulation ($g_{iso} = 2.0052$, $A_{iso}(N) = 1.55$ mT, $A_{iso}(H_\beta) = 1.43$ mT) are characteristic of the DMPO–$^\bullet$OH spin adducts. In comparable reaction conditions, the intensity of the DMPO–$^\bullet$OH EPR signal obtained for $NbCeO_x$ oxide was higher than that for CeO_2, which indicated more abundant production of $^\bullet$OH by the mixed oxide. Notably, no such EPR signal was observed when crystalline Nb_2O_5 was used (spectrum not shown).

The catalysts' ability to activate H_2O_2 towards formation of hydroxyl radicals was also followed by the colorimetric method based on OPD substrate (Sobańska et al., 2017). The corresponding kinetic curves are shown in Fig. 9B, whereas exemplary UV–vis spectra are presented in Fig. S8, Supplementary Data. The intensity of the peak characteristic of 2,3-diaminophenazine (450 nm), the final product of OPD oxidation with hydroxyl radicals, increases steadily with elapsing reaction time. During the reaction without pH control, both $NbCeO_x$ and CeO_2 exhibited high ability to form hydroxyl radicals, while crystalline Nb_2O_5 was inactive in this process, in agreement with the EPR spin trapping results. More pronounced differences in reactivity of $NbCeO_x$ and CeO_2 were observed under acidic conditions. As can be seen in Fig. S9, Supplementary Data, at pH ~ 3 and pH ~ 4, the $NbCeO_x$ oxide catalyst exhibited ca. three times higher activity in $^\bullet$OH generation than that observed for CeO_2. The tests carried out under alkaline conditions (pH ~ 8 and pH ~ 10) revealed that $NbCeO_x$ exhibited negligible activity, while the activity of CeO_2 was comparable to that observed for this material at lower pH values (pH ~ 4). It is worth noting that for $NbCeO_x$ and amorphous Nb_2O_5 CBMM, the absorbance increased with decreasing pH value. In other words, the lower the pH, the higher the number of $^\bullet$OH. Negligible activity of crystalline Nb_2O_5 was observed again at both acidic and basic conditions.

Decomposition of H_2O_2 during interaction with the oxides may also lead to the direct formation of O_2, bypassing the favorable production of ROS. Therefore, the amount of O_2 dissolved in the reaction solution (catalyst/water/hydrogen peroxide assay) was measured with a

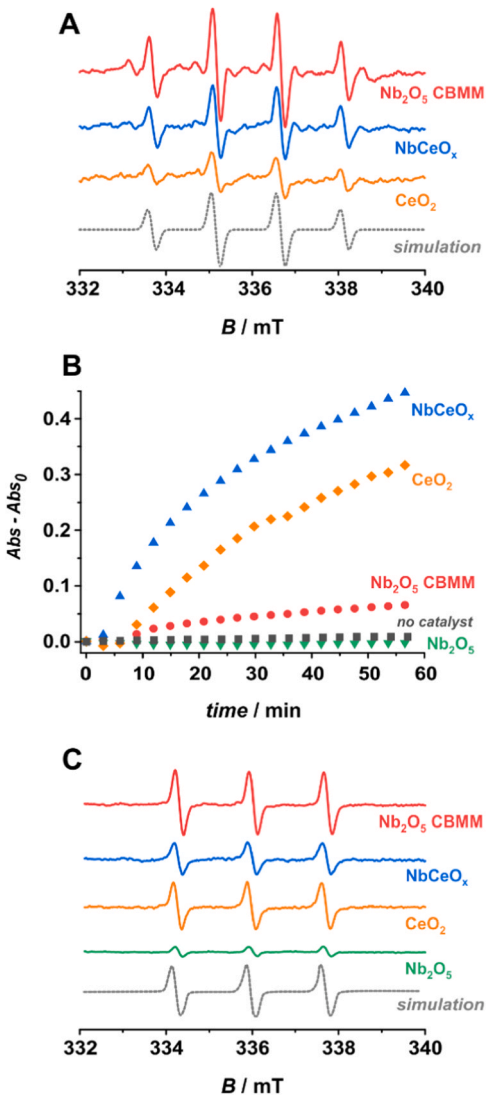


Fig. 9. Treatment of CeO_2, $NbCeO_x$, Nb_2O_5 and Nb_2O_5 CBMM with H_2O_2 in aqueous solution. (A) X-band EPR spectra of spin-trapping experiments with DMPO, (B) kinetic curves based on UV–vis spectra of OPD oxidation without pH control, and (C) EPR spectra of TEMP oxidation to TEMPO.

fluorescence probe. The obtained results (Fig. S10, Supplementary Data) show that the level of dioxygen generation by CeO_2, $NbCeO_x$ and crystalline Nb_2O_5 is quite similar, while the amorphous niobium oxide, Nb_2O_5 CBMM, is the most active. Such observation may not necessary mean the unfavorable loss of H_2O_2 oxidant, as the evolving product may be generated in the excited, singlet spin state ($^1O_2$), known for its high oxidizing potential (Nosaka and Nosaka, 2017; Tang et al., 2020). Therefore, the amount of singlet oxygen was measured indirectly, using the characteristic reaction of selective oxidation of TEMP molecular probe with $^1O_2$, which results in paramagnetic TEMPO (Tang et al., 2020). The latter can be easily detected with EPR. The three-line spectra of TEMPO ($g = 2.0069$, $A_{iso}(N) = 1.73$ mT) formed in situ are shown in Fig. 9C. The highest intensity of the signals measured in the comparable conditions was observed for the amorphous Nb_2O_5 CBMM (in agreement with dissolved O_2 measurements), then for ceria and $NbCeO_x$ (approx. 75% and 44% of Nb_2O_5 CBMM intensity, respectively). Similarly as for the measurements with DMPO spin trapping and OPD oxidation, no activity toward $^1O_2$ formation was observed for crystalline Nb_2O_5.

3.6. Methylene blue degradation

Catalytic activity of the investigated oxides was tested in methylene blue (MB) discoloration, as one of the most intensively studied model reaction based on AOPs with H_2O_2 (Zhao et al., 2012; Prado and Oliveira, 2017). Selection of MB as a model compound is connected with its resistance toward ceria-based catalysts (Wei et al., 2019), while niobia-based catalysts lead to a facile discoloration of MB solutions (Prado and Oliveira, 2017). It was expected that the synergistic interaction between niobium and cerium species may lead to the superior catalytic behavior of the mixed-oxide in this model reaction. Preliminary catalytic tests were performed without pH control and the results obtained are summarized in Fig. 10A (pH values of the reaction mixtures are given in the figure caption). In all the experiments commercial amorphous Nb_2O_5 CBMM was used as a reference material. Considering the reactions without H_2O_2, it was observed that both crystalline CeO_2 and Nb_2O_5 catalysts exhibited very low sorption capacity of the dye. On the other hand, adsorption capacity of the mixed niobium-cerium oxide towards MB was significantly greater than that measured for the other tested oxides. As far as the catalytic activity with H_2O_2 as the ROS precursor is concerned, both CeO_2 and Nb_2O_5 exhibited very low efficiency in MB discoloration (2% and 9% after 40 min of the reaction, respectively). The superior activity of $NbCeO_x$ oxide in this reaction is clearly evidenced by MB discoloration in 83%, as shown in Fig. 10A. Kinetic analyses (Fig. 10B) revealed pseudo-first order character of MB discoloration over all the catalysts studied. For $NbCeO_x$ the estimated reaction rate constant was of 0.0386 min^{-1}, being ca. 3 times higher than the corresponding value obtained for amorphous Nb_2O_5 CBMM, and ca. 240 times higher than for CeO_2 (compare Fig. S11, Supplementary Data). In order to confirm that different activities of the catalysts shown in Fig. 10A do not result from slight differences in pH of the reaction mixtures, the additional kinetic measurements were performed with pH adjusted to 5.1. It appeared that a slight modification of pH had negligible influence on the overall catalysts' activity (Fig. 10C).

To get a deeper insight into the nature of MB discoloration over $NbCeO_x$ catalyst, the UV–vis spectra of the reaction mixtures measured with elapsing time were analyzed (Fig. 10D). The intensity of the band characteristic of MB ($\lambda_{max} = 664$ nm) was significantly reduced after 60 min at the expense of several new bands with the maxima at around 400 and 800 nm. According to literature (Prado and Oliveira, 2017), the former band is characteristic of less complex aromatic compounds formed by the rupture of methylene blue structure, while the latter one is more likely associated with the formation of MB hydroxylation products (compounds formed by substitution/addition of hydroxyl radicals to the structure of MB). Noticeably, the intensity of the band at 400 nm was continuously growing over the reaction time, while the intensity of the band at 800 nm went through a maximum at 60 min, followed by a systematic decline. After 240 min this band almost totally disappeared.

Identification of the products of methylene blue oxidation with H_2O_2 over $NbCeO_x$ was performed with ESI-MS (Fig. 11). For the initial solution, the most intense signal at $m/z = 284$ is attributed to MB molecule, while the less intense signal at $m/z = 270$ is characteristic of partially demethylated molecule (i.e. Azure B (Rauf et al., 2010)). After 1 h of the reaction, the intensity of the peak at $m/z = 284$ was significantly reduced, which was associated with the appearance of several new peaks at $m/z = 345$, 327, 311, 273, 236, 173, 157, and 128. Among them, $m/z = 311$, 327 and 128 were the most intense. All compounds characterized by the above-mentioned peaks were identified, and their proposed structures are shown in Scheme S1 (Supplementary Data). Detailed analysis of the degradation products shows that discoloration of methylene blue was caused by demethylation and hydroxylation of MB molecule followed by the ring rupture process. The mass analysis of the reaction mixture performed after 2 h and 4 h of the reaction revealed that the relative intensities of the mass peaks attributed to almost all identified products were continuously decreasing with the reaction

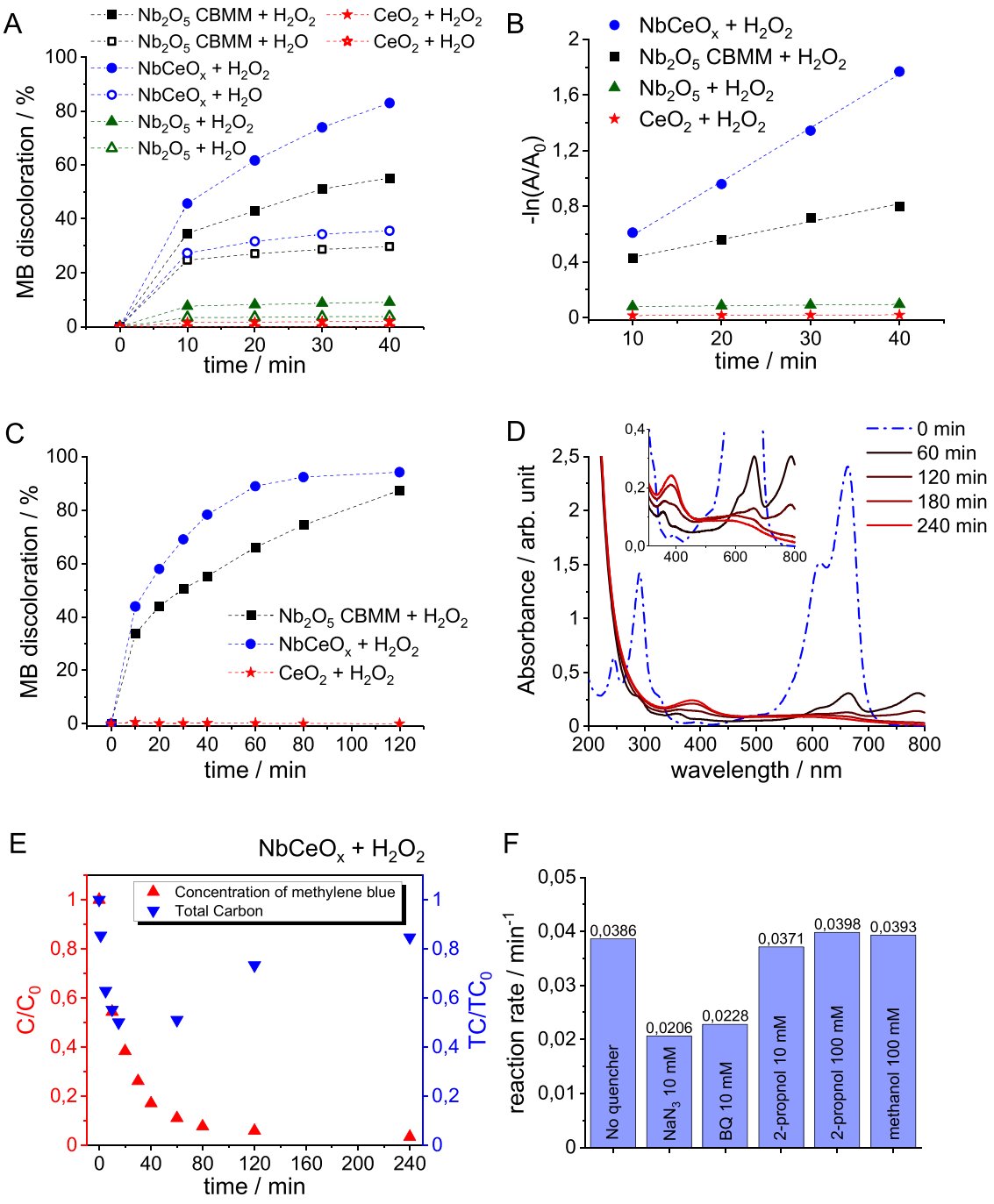


Fig. 10. Methylene blue (MB) discoloration process. (A) Kinetic curves based on UV–vis signal (λ_{max} = 664 nm) obtained without pH control (before addition of H_2O_2 solution, pH values of reaction mixtures were 5.9 for Nb_2O_5 and CeO_2, 5.1 for $NbCeO_x$ and Nb_2O_5 CBMM, respectively; blank symbols: only adsorption, filled symbols: adsorption + degradation), (B) pseudo first order plot for determination of apparent MB discoloration rate without pH control, (C) MB discoloration under pH adjusted to 5.1, (D) UV–vis spectra in progress of MB discoloration with $NbCeO_x$ and H_2O_2, pH = 5.1, (E) comparison of MB discoloration efficiency (C/C_0) and changes in concentration of total carbon (TC/TC_0) ($NbCeO_x$ and H_2O_2, no pH control; pH ~ 5.1), (F) influence of ROS quenchers on MB discoloration rate over $NbCeO_x$ catalyst, pH ~ 5.1.

time, but for some of them the observed intensities were still quite high as in the case of the peak at m/z = 327. Therefore, this peak represents a compound quite stable and difficult to be further oxidized.

Although ESI-MS analyses provided mechanistic insight into MB degradation over $NbCeO_x$, no information on the level of mineralization of the dye was available. To check whether the dye was decolorized or mineralized, the measurements of total carbon (TC) in the reaction mixtures were performed. The results of TC analysis were combined with the results of UV–vis studies (Fig. 10E). During the first 20 min of the reaction, the concentration of MB and the content of TC were coincidently decreasing. After 20 min of the reaction, the concentration of MB was decreasing, but the amount of TC started increasing. One can expect that this phenomenon resulted from the mineralization of organic compounds and formation of inorganic carbon (IC). However, the analysis of inorganic carbon in post reaction mixtures revealed its very low level (almost the same as at the beginning of the reaction). Thus, it was concluded that the increase in concentration of TC resulted from the desorption of the products evolved during partial degradation of MB at

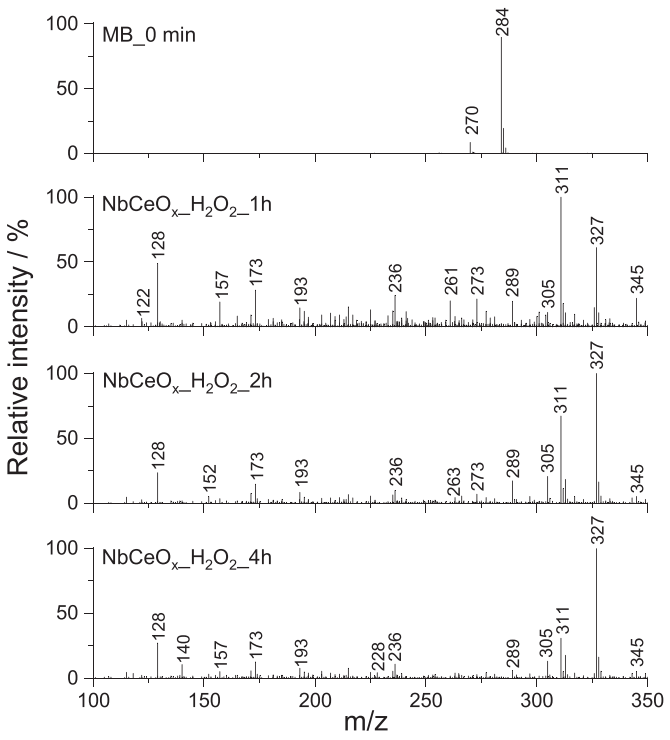


Fig. 11. ESI-MS spectra of MB oxidation with H_2O_2 over $NbCeO_x$ recorded at elapsing reaction time. Reaction conditions: 20 mg of catalyst, 80 mL of methylene blue solution in water (C_{MB} = 12 mg/L), 200 μL of H_2O_2 (30% w/w in H_2O), room temperature, pH ~ 5.1.

the catalyst surface.

4. Discussion

According to literature (Bokare and Choi, 2014; Baldim et al., 2018), one of the most important factors affecting the activity of CeO_2-H_2O_2 system in oxidation of organic molecules is the concentration of Ce^{3+} species. Their reaction with H_2O_2 leads to the formation of surface peroxo groups. Indeed, Raman measurements proved the formation of surface peroxides in the examined materials containing cerium. Additionally, such species were observed on amorphous niobia as well (see Fig. 7). Once formed and adsorbed at the surface, the species can be further transformed into the highly reactive hydroxyl radicals under acidic conditions (induced by H^+ or the presence of surface acidic modifiers, e.g. sulfate groups (Wang et al., 2014)). Alternatively, surface peroxides can react with adsorbed organic molecules leading to their oxidation (Ji et al., 2010; Cai et al., 2010; Chen et al., 2012; Wang et al., 2014). Detailed analysis of XPS data unraveled that the contribution of Ce^{3+} at the surface of CeO_2 was clearly lower than that observed for the mixed niobium-cerium oxide (18% vs. 26% respectively; see Table 1). The increased concentration of Ce^{3+} in the mixed oxide resulted from the presence of the oxo-bridged bimetallic redox centers, namely Nb^{IV}–O–Ce^{IV} ↔ Nb^{V}–O–Ce^{III} electromers, in which both metals can easily change their oxidation states. Note that the existence of two coupled redox pairs Ce^{4+}/Ce^{3+} and Nb^{5+}/Nb^{4+} is a direct consequence of the formation of $CeNbO_4$ phase identified with TEM/SAED. High mobility of electrons in such pair centers was further confirmed by the presence of Nb^{4+} species exclusively in the mixed niobium-cerium oxide (40% of total surface niobium species in $NbCeO_x$ existed in the form of Nb^{4+} cations). It is worth noting that Nb^{5+} cations in monometallic Nb_2O_5 are hardly reducible (Nowak and Ziolek, 1999), in agreement with our XPS results. The presence of Ce^{3+} in $NbCeO_x$ was further confirmed by EPR results (Fig. 8).

High concentration of Ce^{3+} due to the formation of Nb–O–Ce bimetallic redox centers in combination with high acidity of niobium species (increased acidity of $NbCeO_x$, as compared with CeO_2, was assessed with 2-propanol conversion test reaction, Table 2) provide the reasons for high activity of the mixed oxide in the activation of H_2O_2 toward ROS (peroxidase-like activity). This observation has been positively verified with DMPO spin trapping and OPD oxidation test reaction, in which $NbCeO_x$ clearly appeared the most active in $^{\bullet}OH$ generation (Fig. 9A,B).

The most striking difference in the activity of CeO_2 and $NbCeO_x$ catalysts was observed under acidic conditions, i.e. at pH ~ 4 and ~ 3 (see Fig. S9, Supplementary Data). The improved ability of the mixed niobium-cerium oxide to form hydroxyl radicals resulted not only from the presence of the Ce^{3+}/Ce^{4+} redox couple, but also from the cooperative behavior of Nb species. We have shown previously that the surface of Nb_2O_5 is active in the electroprotic decomposition of H_2O_2 and simultaneous generation of superoxide and hydroxyl radicals at acidic pH close to the isoelectric point of the oxide (Ziolek et al., 2015). This type of reactivity is featured with the reaction:

$$H_2O_{2(aq)} + HO^-_{2(aq)} = O_2^{\bullet-}{}_{(aq)} + {}^{\bullet}OH_{(aq)} + H_2O, \quad (1)$$

followed by trapping of the radicals by surface Nb(V) centers:

$$O_2^{\bullet-}{}_{(aq)} + Nb_2O_5/Nb^{5+}{}_{(surf)} = Nb_2O_5/Nb^{5+}\text{–}O_2^{\bullet-}{}_{(surf)} \quad (2)$$

and formation of stable surface superoxides. Moreover, the surface of Nb_2O_5 becomes covered with peroxide species with increasing pH. Indeed, in this study the paramagnetic superoxide species were observed not only for the amorphous Nb_2O_5 CBMM (as expected), but also for the $NbCeO_x$ catalyst as evidenced by the solid-state EPR spectra (Fig. 8). The spectrum characteristic of these species was not observed for CeO_2. At the same time, peroxo species were found with micro-Raman measurements on the surface of amorphous Nb_2O_5 CBMM, $NbCeO_x$ and CeO_2 as well. Therefore, it is plausible that high activity of the mixed oxide in ROS generation originated from the synergy between niobium and cerium. Decreasing activity of $NbCeO_x$ in OPD oxidation with increasing pH (see Fig. 9B and Fig. S9) suggests a minor role of free $^{\bullet}OH$ radicals (see below), whereas the stable activity of CeO_2 toward OPD with increasing pH (up to 8–9) suggests that the surface peroxides are stabilized on cerium sites as the possible precursors for $^{\bullet}OH$ formation.

Such observations indicate that the properties of both niobium and cerium species in the mixed $NbCeO_x$ oxide differ significantly from those observed for the parent crystalline CeO_2 and Nb_2O_5 phases. In particular, no activity in OPD oxidation, peroxide or superoxide formation upon interaction with H_2O_2 was observed for crystalline Nb_2O_5. Thus, the results of the test reactions prove that $NbCeO_x$ cannot be considered as a simple composite consisting of Nb_2O_5 and CeO_2. Such a conclusion is in agreement with the presence of the new $CeNbO_4$ phase identified by electron diffraction and the observed narrowing of the electronic band gap (as compared with that of both parent oxides). Altogether, the experimental evidence has shown that the mixed oxide has to be considered as a new material of high peroxidase-like activity toward H_2O_2.

Previous literature data clearly show that chemical degradation of the dyes' molecules by the CeO_2-H_2O_2 system is an adsorption-triggered process (Ji et al., 2010; Cai et al., 2010; Chen et al., 2012; Wang et al., 2014). Indeed, as can be seen in Fig. 10A,C, CeO_2 exhibited very low ability to adsorb MB and, consequently, very low activity in the discoloration of the dye solution, although formation of $^{\bullet}OH$ was observed under the same reaction conditions (compare Fig. 9). The significance of the adsorption step in the degradation of MB can be clearly observed for the mixed oxide catalyst. Fig. 10A shows that $NbCeO_x$ exhibited very high ability for MB adsorption. This observation can be traced back to the combined effect of high surface area and significant surface acidity. Even though both CeO_2 and $NbCeO_x$ exhibited activity in $^{\bullet}OH$ generation (Fig. 9A,B), it is the mixed catalyst which significantly outperformed ceria in the discoloration of MB solution.

Noticeably, the activity of $NbCeO_x$ was higher than that observed for the commercial amorphous Nb_2O_5 CBMM, which had a similar capacity for adsorption of MB and exhibited peroxidase-like activity owing to the electroprotic mechanism discussed above.

In view of these findings, $NbCeO_x$ catalyst seems to be active in the degradation of MB not only owing to the formation of hydroxyl radicals (as previously established for the niobia-based systems (Prado and Oliveira, 2017)), but there has to be an alternative pathway that contributes to such an efficient discoloration process. Indeed, the combined TC and UV–vis studies (see Fig. 10E) proved that the degradation of MB was preceded by its sorption. The synergy between adjacent niobium and cerium species, established with XPS, EPR and TEM methods, allows the cooperative action of niobium (stabilization of surface superoxides and foundation of the adsorption Lewis/Brønsted acidic sites for MB molecules) and cerium (production of the peroxide species and hydroxyl radicals) on the surface of $NbCeO_x$ oxide. A close distance between the adsorbed organic molecules and the surface-stabilized ROS is one of the key factors promoting oxidation of the dye molecules according to the adsorption-triggered process (Ji et al., 2010; Cai et al., 2010; Chen et al., 2012; Wang et al., 2014).

The efficiency of methylene blue discoloration over the mixed Nb-Ce oxide is more likely boosted by the presence of the oxo-bridged bimetallic Nb-O-Ce sites, which act as the redox and adsorption centers discussed above. Yet, it cannot be excluded that some of the dye molecules could be directly oxidized in a liquid phase by hydroxyl radicals formed over the mixed niobium-cerium oxide. To support this conjecture, the effect of ROS quenchers was studied (Fig. 10F and Figs. S12–13, Supplementary Data). The impact of 2-propanol and methanol (typical scavengers of hydroxyl radicals) is negligible. This suggests elusive involvement of free $^{\bullet}OH$ in the oxidation of MB and points out the importance of surface transformations of co-adsorbed ROS and MB. Detailed analysis of the contribution of the surface process and liquid phase process requires further studies, but the results obtained in this work clearly show that the surface process plays the most important role in the discoloration of MB solution over the mixed oxide.

As mentioned above, strong interaction between niobium and cerium species in the mixed oxide brought about a significant increase in the relative concentration of Ce^{3+} ions when compared to monometallic CeO_2. The surface Ce^{3+} cations can react with hydrogen peroxide leading to the formation of peroxide species. We observed that the intensity of Ce^{3+} EPR signal measured for the mixed oxide was significantly reduced after the treatment of $NbCeO_x$ with H_2O_2. This effect resulted more likely from the partial oxidation of Ce^{3+} by H_2O_2 connected with the formation of $O_2^{-\bullet}$ (evidenced by EPR) and, in a further step, O_2^{2-} (probed with Raman). The newly formed peroxo species can be stabilized by the remaining Ce^{3+}. At the same time, MB molecules remain chemisorbed on the vicinal niobium centers of the bimetallic Nb^{V}–O–Ce^{III} active site. In such conditions the peroxo species are further transformed into the hydroxyl radicals (Zang et al., 2018), which eventually are responsible for the first steps of the degradation of MB (see initial products of $m/z = 345$, 327, 311 identified with ESI-MS, Scheme S1, Supplementary Data). Yet, another source of $^{\bullet}OH$ radicals is reaction (1), which requires the participation of Nb(V) centers. This reaction can only be effective on the surface, since one of the products, namely superoxo radical, can only be stabilized on the surface (reaction (2)). As a result, the presence of both surface peroxo and superoxo groups, formed in a close proximity to niobium species, playing the role of adsorption sites for MB molecules, is more likely responsible for triggering the oxidation reaction.

Apart from ROS formation, all oxides which were active in MB discoloration led to the decomposition of H_2O_2 and production of dioxygen, as follows from the measurements of dissolved O_2 with a photoluminescent probe (Fig. S10, Supplementary Data). Such a reaction partially resulted in the production of singlet oxygen in which CeO_2 and the commercial amorphous Nb_2O_5 CBMM were the most active (Fig. 9C). The role of $^1O_2$ in the oxidation of MB may also be important for $NbCeO_x$, as the measurements of the MB discoloration process in the presence of NaN_3 showed a decrease in the observed reaction rate by 47% (Fig. 10F). A similar effect was obtained for benzoquinone, BQ, a scavenger of superoxide radicals. We postulate that a mutual influence of $^1O_2$ and $O_2^{-\bullet}$ is related to the presence of the mixed-valent Nb–O–Ce bimetallic centers. The reduced cations could be responsible for electron capture from superoxide and formation of singlet oxygen. The resulting electron shuffle leads to the re-oxidation of the bimetallic centers or activation of the surface peroxides and subsequent formation of hydroxyl radicals, as discussed above.

5. Conclusions

A thorough structural and chemical characterization of the mixed niobium-cerium $NbCeO_x$ oxide and its reactivity in methylene blue degradation upon H_2O_2 was made. On the basis of the structural studies, the binary $CeNbO_4$ phase was identified together with tightly agglomerated phases of CeO_2 and Nb_2O_5. The electronic structure of $NbCeO_x$ was clearly influenced by a strong synergy between niobium and cerium. The presence of reduced Nb(IV) and Ce(III) species, which formed oxo-bridged bimetallic redox centers Nb^{IV}–O–Ce^{IV} ↔ Nb^{V}–O–Ce^{III} in the mixed oxide, was revealed at significantly higher concentrations than those for pristine CeO_2 and Nb_2O_5. Well-developed surface of $NbCeO_x$ catalyst exhibited mixed redox-acidic nature, constituting convenient conditions for the efficient adsorption of molecules of both H_2O_2 and methylene blue. Owing to the presence of Ce^{3+}/Ce^{4+} and Nb^{4+}/Nb^{5+} redox pairs, $NbCeO_x$ was the most active in OPD oxidation with hydroxyl radicals. It was found that the interaction with H_2O_2 led to the formation of both peroxo and superoxo species stabilized on $NbCeO_x$ surface. In the case of ceria, only peroxo species were observed. The mechanistic insight into the oxidative degradation of MB with H_2O_2 revealed that it was an adsorption-triggered process. The degradation of adsorbed MB was initiated by hydroxyl radicals generated in situ on the surface from the peroxo/superoxo precursors. Apart from this pathway, the involvement of singlet oxygen was clearly shown. The overall catalytic activity of $NbCeO_x$ was higher than that observed for the commercial amorphous niobia (Nb_2O_5 CBMM), which had a similar capacity for the adsorption of MB as $NbCeO_x$. Additionally, the mixed oxide significantly outperformed CeO_2. The latter, even though well-known for its Fenton-like reactivity, appeared inert toward degradation of MB with H_2O_2. The observed high activity of $NbCeO_x$ was attributed to the concerted effects of the Fenton-like and electroprotic generation of ROS along with the effective adsorption of the dye molecules. Both factors originated from the synergy between niobium and cerium species.

CRediT authorship contribution statement

Lukasz Wolski: Conceptualization, Methodology, Validation, Investigation, Resources, Data curation, Writing - original draft, Writing - review & editing, Visualization, Funding acquisition, Project administration. **Kamila Sobańska:** Methodology, Validation, Investigation, Data curation, Visualization, Writing - original draft. **Adrian Walkowiak:** Investigation, Data curation. **Kamila Akhmetova:** Investigation, Data curation. **Joanna Gryboś:** Methodology, Validation, Investigation, Data curation, Visualization. **Marcin Frankowski:** Methodology, Validation, Investigation, Data curation. **Maria Ziolek:** Conceptualization, Resources, Writing - review & editing, Supervision. **Piotr Pietrzyk:** Conceptualization, Methodology, Validation, Investigation, Resources, Data curation, Writing - review & editing, Funding acquisition, Project administration, Supervision.

Declaration of Competing Interest

The authors declare that they have no known competing financial interests or personal relationships that could have appeared to influence the work reported in this paper.

Acknowledgments

This paper is a result of a collaborative research financially supported by the National Science Center, Poland (NCN), grants Sonatina2 2018/28/C/ST5/00255 and Sonata Bis7 2017/26/E/ST4/00794. K. Akhmetova thanks for the scholarship from ASC Master's Course financed by Erasmus+EMJMD programme.

Appendix A. Supporting information

Supplementary data associated with this article can be found in the online version at doi:10.1016/j.jhazmat.2021.125665.

References

Aboukaïs, A., Skaf, M., Hany, S., Cousin, R., Aouad, S., Labaki, M., Abi-Aad, E., 2016. A comparative study of Cu, Ag and Au doped CeO_2 in the total oxidation of volatile organic compounds (VOCs). Mater. Chem. Phys. 177, 570–576. https://doi.org/10.1016/j.matchemphys.2016.04.072.

Ansari, S.A., Khan, M.M., Ansari, M.O., Kalathil, S., Lee, J., Cho, M.H., 2014. Band gap engineering of CeO_2 nanostructure using an electrochemically active biofilm for visible light applications. RSC Adv. 4, 16782–16791. https://doi.org/10.1039/c4ra00861h.

Artini, C., Pani, M., Carnasciali, M.M., Buscaglia, M.T., Plaisier, J.R., Costa, G.A., 2015. Structural features of Sm- and Gd-doped ceria studied by synchrotron X-ray diffraction and μ-Raman spectroscopy. Inorg. Chem. 54, 4126–4137. https://doi.org/10.1021/acs.inorgchem.5b00395.

Baldim, V., Bedioui, F., Mignet, N., Margaill, I., Berret, J.F., 2018. The enzyme-like catalytic activity of cerium oxide nanoparticles and its dependency on Ce^{3+} surface area concentration. Nanoscale 10, 6971–6980. https://doi.org/10.1039/c8nr00325d.

Bêche, E., Charvin, P., Perarnau, D., Abanades, S., Flamant, G., 2008. Ce 3d XPS investigation of cerium oxides and mixed cerium oxide ($Ce_xTi_yO_z$). Surf. Interface Anal. 40, 264–267. https://doi.org/10.1002/sia.2686.

Bokare, A.D., Choi, W., 2014. Review of iron-free Fenton-like systems for activating H_2O_2 in advanced oxidation processes. J. Hazard. Mater. 275, 121–135. https://doi.org/10.1016/j.jhazmat.2014.04.054.

Brayner, R., Bozon-Verduraz, F., 2003. Niobium pentoxide prepared by soft chemical routes: morphology, structure, defects and quantum size effect. Phys. Chem. Chem. Phys. 5, 1457–1466. https://doi.org/10.1039/b210055j.

Cai, W., Chen, F., Shen, X., Chen, L., Zhang, J., 2010. Enhanced catalytic degradation of AO7 in the CeO_2-H_2O_2 system with Fe^{3+} doping. Appl. Catal. B Environ. 101, 160–168. https://doi.org/10.1016/j.apcatb.2010.09.031.

Cardoso, F.P., Nogueira, A.E., Patrício, P.S.O., Oliveira, L.C.A., 2012. Effect of tungsten doping on catalytic properties of niobium oxide. J. Braz. Chem. Soc. 23, 702–709.

Chen, B.B., Shi, C., Crocker, M., Wang, Y., Zhu, A.M., 2013. Catalytic removal of formaldehyde at room temperature over supported gold catalysts. Appl. Catal. B Environ. 132–133, 245–255. https://doi.org/10.1016/j.apcatb.2012.11.028.

Chen, F., Shen, X., Wang, Y., Zhang, J., 2012. CeO_2/H_2O_2 system catalytic oxidation mechanism study via a kinetics investigation to the degradation of acid orange 7. Appl. Catal. B Environ. 121–122, 223–229. https://doi.org/10.1016/j.apcatb.2012.04.014.

Cui, Z., Zhou, H., Wang, G., Zhang, Y., Zhang, H., Zhao, H., 2019. Enhancement of the visible-light photocatalytic activity of CeO_2 by chemisorbed oxygen in the selective oxidation of benzyl alcohol. New J. Chem. 43, 7355–7362. https://doi.org/10.1039/c9nj01098j.

Díaz-Uribe, C.E., Vallejo-Lozada, W.A., Martinez-Ortega, F., 2014. Photooxidation of anthracene under visible light with metallocarboxyphenylporphyrins. Rev. Fac. Ing. Univ. Antioquia. 73, 225–230.

Gervasini, A., Fenyvesi, J., Auroux, A., 1997. Study of the acidic character of modified metal oxide surfaces using the test of isopropanol decomposition. Catal. Lett. 43, 219–228. https://doi.org/10.1023/A:1018979731407.

Hamoud, I.H., Finqueneisel, G., Azambre, B., 2017. Removal of binary dyes mixtures with opposite and similar charges by adsorption, coagulation/flocculation and catalytic oxidation in the presence of CeO_2/H_2O_2 Fenton-like system. J. Environ. Manag. 195, 195–207. https://doi.org/10.1016/j.jenvman.2016.07.067.

Ji, P., Wang, L., Chen, F., Zhang, J., 2010. Ce^{3+}-centric organic pollutant elimination by CeO_2 in the presence of H_2O_2. ChemCatChem. 2, 1552–1554. https://doi.org/10.1002/cctc.201000191.

Kim, H.Y., Lee, H.M., Henkelman, G., 2012. CO oxidation mechanism on CeO_2-supported Au nanoparticles. J. Am. Chem. Soc. 134, 1560–1570. https://doi.org/10.1021/ja207510v.

Kong, L., Zhang, C., Wang, J., Qiao, W., Ling, L., Long, D., 2016. Nanoarchitectured Nb_2O_5 hollow, Nb_2O_5@carbon and NbO_2@carbon core-shell microspheres for ultrahigh-rate intercalation pseudocapacitors. Sci. Rep. 6, 21177. https://doi.org/10.1038/srep21177.

Lahousse, C., Bachelier, J., Lavalley, J.C., Lauron-Pernot, H., Govic, A.M. Le, 1994. Validity of using isopropanol decomposition as a test-reaction for the characterization of metal oxides basicity; comparison with results obtained from methylbutynol decomposition. J. Mol. Catal. 87, 329–332. https://doi.org/10.1016/0304-5102(93)E0232-6.

Łańcucki, Ł., Kruczała, K., 2014. Development of stabilized protonconducting membrane based on poly(ethylene-co-vinyl alcohol). Polym. Degrad. Stab. 109, 327–335. https://doi.org/10.1016/j.polymdegradstab.2014.08.002.

Li, S., Schmidt, C.N., Xu, Q., Cao, X., Cao, G., 2016. Macroporous nanostructured Nb_2O_5 with surface Nb^{4+} for enhanced lithium ion storage properties. ChemNanoMat. 2, 675–680. https://doi.org/10.1002/cnma.201600101.

Liang, M., Yan, X., 2019. Nanozymes: from new concepts, mechanisms, and standards to applications. Acc. Chem. Res. 52, 2190–2200. https://doi.org/10.1021/acs.accounts.9b00140.

Liu, H., Gao, N., Liao, M., Fang, X., 2015. Hexagonal-like Nb_2O_5 nanoplates-based photodetectors and photocatalyst with high performances. Sci. Rep. 5, 7716. https://doi.org/10.1038/srep07716.

Liu, L., Yao, Z., Liu, B., Dong, L., 2010. Correlation of structural characteristics with catalytic performance of CuO/$Ce_xZr_{1-x}O_2$ catalysts for NO reduction by CO. J. Catal. 275, 45–60. https://doi.org/10.1016/j.jcat.2010.07.024.

Liu, Y., Luo, L., Gao, Y., Huang, W., 2016. CeO_2 morphology-dependent NbO_x–CeO_2 interaction, structure and catalytic performance of NbO_x/CeO_2 catalysts in oxidative dehydrogenation of propane. Appl. Catal. B Environ. 197, 214–221. https://doi.org/10.1016/j.apcatb.2016.03.011.

Majumder, D., Chakraborty, I., Mandal, K., Roy, S., 2019. Facet-dependent photodegradation of methylene blue using pristine CeO_2 nanostructures. ACS Omega 4, 4243–4251. https://doi.org/10.1021/acsomega.8b03298.

Maslakov, K.I., Teterin, Y.A., Popel, A.J., Teterin, A.Y., Ivanov, K.E., Kalmykov, S.N., Petrov, V.G., Petrov, P.K., Farnan, I., 2018. XPS study of ion irradiated and unirradiated CeO_2 bulk and thin film samples. Appl. Surf. Sci. 448, 154–162. https://doi.org/10.1016/j.apsusc.2018.04.077.

Montini, T., Melchionna, M., Monai, M., Fornasiero, P., 2016. Fundamentals and catalytic applications of CeO_2-based materials. Chem. Rev. 116, 5987–6041. https://doi.org/10.1021/acs.chemrev.5b00603.

Nakamura, R., Okamoto, A., Osawa, H., Irie, H., Hashimoto, K., 2007. Design of all-inorganic molecular-based photocatalysts sensitive to visible light: Ti(IV)-O-Ce(III) bimetallic assemblies on mesoporous silica. J. Am. Chem. Soc. 129, 9596–9597. https://doi.org/10.1021/ja073668n.

Nosaka, Y., Nosaka, A.Y., 2017. Generation and detection of reactive oxygen species in photocatalysis. Chem. Rev. 117, 11302–11336. https://doi.org/10.1021/acs.chemrev.7b00161.

Nowak, I., Jaroniec, M., 2008. "Hard" vs. "soft" templating synthesis of mesoporous Nb_2O_5 catalysts for oxidation reactions. Top. Catal. 49, 193–203. https://doi.org/10.1007/s11244-008-9084-1.

Nowak, I., Ziolek, M., 1999. Niobium compounds: preparation, characterization, and application in heterogeneous catalysis. Chem. Rev. 99, 3603–3624.

Okamoto, A., Nakamura, R., Osawa, H., Hashimoto, K., 2008. Site-specific synthesis of oxo-bridged mixed-valence binuclear complexes on mesoporous silica. Langmuir. 24, 7011–7017. https://doi.org/10.1021/la704032c.

Oliveira, L.C.A., Gonçalves, M., Guerreiro, M.C., Ramalho, T.C., Fabris, J.D., Pereira, M. C., Sapag, K., 2007. A new catalyst material based on niobia/iron oxide composite on the oxidation of organic contaminants in water via heterogeneous Fenton mechanisms. Appl. Catal. A Gen. 316, 117–124. https://doi.org/10.1016/j.apcata.2006.09.027.

Ong, S.-A., Ho, L.-N., Wong, Y.-S., Zainuddin, A., 2013. Adsorption behavior of cationic and anionic dyes onto acid treated coconut coir. Sep. Sci. Technol. 48, 2125–2131. https://doi.org/10.1080/01496395.2013.792839.

Pereira-Hernández, X.I., DeLaRiva, A., Muravev, V., Kunwar, D., Xiong, H., Sudduth, B., Engelhard, M., Kovarik, L., Hensen, E.J.M., Wang, Y., Datye, A.K., 2019. Tuning Pt-CeO_2 interactions by high-temperature vapor-phase synthesis for improved reducibility of lattice oxygen. Nat. Commun. 10, 1358. https://doi.org/10.1038/s41467-019-09308-5.

Prado, N.T., Oliveira, L.C.A., 2017. Nanostructured niobium oxide synthetized by a new route using hydrothermal treatment: High efficiency in oxidation reactions. Appl. Catal. B Environ. 205, 481–488. https://doi.org/10.1016/j.apcatb.2016.12.067.

Qu, R., Gao, X., Cen, K., Li, J., 2013. Relationship between structure and performance of a novel cerium-niobium binary oxide catalyst for selective catalytic reduction of NO with NH_3. Appl. Catal. B Environ. 142–143, 290–297. https://doi.org/10.1016/j.apcatb.2013.05.035.

Rauf, M.A., Meetani, M.A., Khaleel, A., Ahmed, A., 2010. Photocatalytic degradation of methylene blue using a mixed catalyst and product analysis by LC/MS. Chem. Eng. J. 157, 373–378. https://doi.org/10.1016/j.cej.2009.11.017.

Reddy, B.M., Bharali, P., Saikia, P., Park, S.E., Van Den Berg, M.W.E., Muhler, M., Grünert, W., 2008. Structural characterization and catalytic activity of nanosized $Ce_xM_{1-x}O_2$ (M = Zr and Hf) mixed oxides. J. Phys. Chem. C 112, 11729–11737. https://doi.org/10.1021/jp802674m.

Santoro, A., Marezio, M., Roth, R.S., Minor, D., 1980. Neutron powder diffraction study of the structures of $CeTaO_4$, $CeNbO_4$, and $NdTaO_4$. J. Solid State Chem. 35, 167–175. https://doi.org/10.1016/0022-4596(80)90489-2.

Schilling, C., Hofmann, A., Hess, C., Ganduglia-Pirovano, M.V., 2017. Raman spectra of polycrystalline CeO_2: a density functional theory study. J. Phys. Chem. C 121, 20834–20849. https://doi.org/10.1021/acs.jpcc.7b06643.

Sobańska, K., Krasowska, A., Mazur, T., Podolska-Serafin, K., Pietrzyk, P., Sojka, Z., 2015. Diagnostic features of EPR spectra of superoxide intermediates on catalytic surfaces and molecular interpretation of their G and A tensors. Top. Catal. 58, 796–810. https://doi.org/10.1007/s11244-015-0420-y.

Sobańska, K., Pietrzyk, P., Sojka, Z., 2017. Generation of reactive oxygen species via electroprotic interaction of H_2O_2 with ZrO_2 gel: ionic sponge effect and ph-switchable peroxidase- and catalase-like activity. ACS Catal. 7, 2935–2947. https://doi.org/10.1021/acscatal.7b00189.

Souza, J.P., Melo, T., De Oliveira, M.A.L., Paniago, R.M., De Souza, P.P., Oliveira, L.C.A., 2012. Applied Catalysis A: vgeneral V- or Mo-modified niobium catalysts for glycerin conversion reactions in the presence of H_2O_2. Applied Catal. A Gen. 443–444, 153–160. https://doi.org/10.1016/j.apcata.2012.07.041.

Spałek, T., Pietrzyk, P., Sojka, Z., 2005. Application of the genetic algorithm joint with the powell method to nonlinear least-squares fitting of powder EPR spectra. J. Chem. Inf. Model. 45, 18–29. https://doi.org/10.1021/ci049863s.

Stošić, D., Bennici, S., Rakić, V., Auroux, A., 2012. CeO_2–Nb_2O_5 mixed oxide catalysts: preparation, characterization and catalytic activity in fructose dehydration reaction. Catal. Today. 192, 160–168. https://doi.org/10.1016/j.cattod.2011.10.040.

Sun, X., Lin, J., 2009. Synergetic effects of thermal and photo-catalysis in purification of dye water over $SrTi_{1-x}Mn_xO_3$ solid solutions. J. Phys. Chem. C 113, 4970–4975. https://doi.org/10.1021/jp810227y.

Tamai, K., Hosokawa, S., Teramura, K., Shishido, T., Tanaka, T., 2016. Synthesis of niobium oxide nanoparticles with plate morphology utilizing solvothermal reaction and their performances for selective photooxidation. Appl. Catal. B Environ. 182, 469–475. https://doi.org/10.1016/j.apcatb.2015.10.003.

Tang, S., Wang, Z., Yuan, D., Zhang, C., Rao, Y., Wang, Z., Yin, K., 2020. Ferrous ion-tartaric acid chelation promoted calcium peroxide fenton-like reactions for simulated organic wastewater treatment. J. Clean. Prod. 268, 122253 https://doi.org/10.1016/j.jclepro.2020.122253.

Thommes, M., Kaneko, K., Neimark, A.V., Olivier, J.P., Rodriguez-Reinoso, F., Rouquerol, J., Sing, K.S.W., 2015. Physisorption of gases, with special reference to the evaluation of surface area and pore size distribution (IUPAC Technical Report). Pure Appl. Chem. 87, 1051–1069. https://doi.org/10.1515/pac-2014-1117.

Wachs, I.E., Roberts, C.A., 2010. Monitoring surface metal oxide catalytic active sites with Raman spectroscopy. Chem. Soc. Rev. 39, 5002–5017. https://doi.org/10.1039/c0cs00145g.

Wang, F., Wei, M., Evans, D.G., Duan, X., 2016. CeO_2-based heterogeneous catalysts toward catalytic conversion of CO_2. J. Mater. Chem. A 4, 5773–5783. https://doi.org/10.1039/c5ta10737g.

Wang, Y., Shen, X., Chen, F., 2014. Improving the catalytic activity of CeO_2/H_2O_2 system by sulfation pretreatment of CeO_2. J. Mol. Catal. A Chem. 381, 38–45. https://doi.org/10.1016/j.molcata.2013.10.003.

Wei, X., Wang, Y., Feng, Y., Xie, X., Li, X., Yang, S., 2019. Different adsorption-degradation behavior of methylene blue and Congo red in nanoceria/H_2O_2 system under alkaline conditions. Sci. Rep. 9, 2–11. https://doi.org/10.1038/s41598-018-36794-2.

Yang, W., Wang, X., Song, S., Zhang, H., 2019. Syntheses and applications of noble-metal-free CeO_2-based mixed-oxide nanocatalysts. Chem 5, 1743–1774. https://doi.org/10.1016/j.chempr.2019.04.009.

You, R., Zhang, X., Luo, L., Pan, Y., Pan, H., Yang, J., Wu, L., Zheng, X., Jin, Y., Huang, W., 2017. NbO_x/CeO_2-rods catalysts for oxidative dehydrogenation of propane: Nb–CeO_2 interaction and reaction mechanism. J. Catal. 348, 189–199. https://doi.org/10.1016/j.jcat.2016.12.012.

Zang, C., Yu, K., Hu, S., Chen, F., 2018. Adsorption-depended Fenton-like reaction kinetics in CeO_2-H_2O_2 system for salicylic acid degradation. Colloids Surf. A Physicochem. Eng. Asp. 553, 456–463. https://doi.org/10.1016/j.colsurfa.2018.05.100.

Zhang, C., Lin, J., 2011. Visible-light induced oxo-bridged Zr^{IV}-O-Ce^{III} redox centre in tetragonal ZrO_2-CeO_2 solid solution for degradation of organic pollutants. Phys. Chem. Chem. Phys. 13, 3896–3905. https://doi.org/10.1039/c0cp01782e.

Zhao, Y., Eley, C., Hu, J., Foord, J.S., Ye, L., He, H., Tsang, S.C.E., 2012. Shape-dependent acidity and photocatalytic activity of Nb_2O_5 nanocrystals with an active TT (001) surface. Angew. Chem. Int. Ed. 51, 3846–3849. https://doi.org/10.1002/anie.201108580.

Ziolek, M., Golinska-Mazwa, H., Filipek, E., Piz, M., 2012. Catalytic properties of new ternary Nb-Sb-V oxide - a comparative study with mechanical mixture of single oxides and binary systems. Catal. Today 187, 159–167. https://doi.org/10.1016/j.cattod.2011.10.038.

Ziolek, M., Sobczak, I., Decyk, P., Sobańska, K., Pietrzyk, P., Sojka, Z., 2015. Search for reactive intermediates in catalytic oxidation with hydrogen peroxide over amorphous niobium(V) and tantalum(V) oxides. Appl. Catal. B Environ. 164, 288–296. https://doi.org/10.1016/j.apcatb.2014.09.024.